Submitted to The Astrophysical Journal

History of Galaxy Interactions and Their Impact on Star Formation over the Last 7 Gyr from GEMS

Shardha Jogee [1], Sarah H. Miller [1], Kyle Penner [1], Rosalind E. Skelton [3], Chris Conselice [2], Rachel S. Somerville [3], Eric F.Bell [3], Xian Zhong Zheng [16], Hans-Walter Rix [3], Aday R. Robaina [3], Fabio D. Barazza [6], Marco Barden [15], Andrea Borch [3], Steven V.W. Beckwith [5], John A. R.Caldwell [7], Boris Häußler [2], Catherine Heymans [13,14], Knud Jahnke [3], Daniel H. McIntosh [8], Klaus Meisenheimer [3], Casey Papovich [4], Chien Y. Peng [9], Sebastian F. Sanchez [10], Lutz Wisotzki [11], Christian Wolf [12]

sj@astro.as.utexas.edu

ABSTRACT

We explore the frequency and impact of interactions on the star formation rate (SFR) of galaxies over $z \sim 0.24$–0.80 (lookback time $\sim$ 3–7 Gyr), based on *HST* ACS, Combo-17, and Spitzer 24 μm data of $\sim$ 3690 ($M \geq 1 \times 10^9\ M_\odot$) galaxies in the GEMS survey. Two independent methods are used to identify interacting galaxies: a tailored visual classification system complemented with spectrophotometric redshifts and stellar masses, as well as the CAS merger criterion ($A > 0.35$ and $A > S$). of mass ratio $M1/M2 > 1/10$. Our results are: (1) The fraction f of visually-classified interacting systems among high mass

[1]Department of Astronomy, University of Texas at Austin, 1 University Station C1400, Austin, TX 78712-0259

[2]School of Physics and Astronomy, The University of Nottingham, University Park, Nottingham NG7 2RD, UK

[3]Max-Planck-Institut für Astronomie, Königstuhl 17, D-69117, Heidelberg, Germany

[4]Department of Astronomy, University of Arizona, Steward Observatory, 933 N. Cherry Avenue, Tucson, AZ 85721

[5]Department of Physics and Astronomy, Johns Hopkins University, Charles and 4th Street, Baltimore, MD 21218

[6]Laboratoire d'Astrophysique, École Polytechnique Fédérale de Lausanne (EPFL), Observatoire, 1290 Sauverny, Switzerland

[7]University of Texas, McDonald Observatory, Fort Davis TX, 79734 USA

[8]Department of Astronomy, University of Massachusetts, 710 North Pleasant Street, Amherst, MA 01003, USA

[9]NRC Herzberg Institute of Astrophysics, Victoria, Canada

[10]Centro Astronmico Hispano Alemn, Calar Alto, CSIC-MPG, C/Jess Durbn Remn 2-2, E-04004 Almeria, Spain

[11]Astrophysikalisches Institut Potsdam, An der Sternwarte 16, D-14482 Potsdam, Germany

[12]Astrophysics, University of Oxford, Keble Road, Oxford OX1 3RH, U.K.

[13]Department of Physics and Astronomy, University of British Columbia, 6224 Agricultural Road, Vancouver, V6T 1Z1, Canada

[14]Institut d'Astrophysique de Paris, UMR7095 CNRS, 98 bis bd Arago, 75014 Paris, France

[15]Institute for Astro- and Particle Physics, University of Innsbruck, Technikerstr. 25/8, A-6020 Innsbruck, Austria

[16]Purple Mountain Observatory, Nanjing, China.

($M \geq 2.5 \times 10^{10}$ $M_{\odot}$) galaxies remains fairly constant over $z \sim 0.24$–0.80, ranging from $9\% \pm 5\%$ at $z \sim 0.24$–0.34, to $8\% \pm 2\%$ at $z \sim 0.60$–0.80. The major merger fraction has a lower limit ranging from $1.1\% \pm 0.1\%$ to $3.5\% \pm 2.2\%$ over $z \sim 0.24$–0.80. The corresponding lower limit for the minor merger fraction is $3.6\% \pm 2.2\%$ to $7.5\% \pm 2.7\%$. For an assumed visibility timescale of ~ 0.5 Gyr, it follows that each massive galaxy has undergone at least 0.7 interactions of mass ratio $> 1/10$ since $z < 0.8$, with at least 0.19 being major mergers, and 0.44 being minor mergers. The interaction rate R is $\sim$ a few $\times 10^{-4}$ galaxies Gyr^{-1} Mpc^{-3}. Similar results are found for blue cloud intermediate mass ($M \geq 1.0 \times 10^{9}$ $M_{\odot}$) galaxies. (2) We compare our interaction fraction f and rate R to predictions from different ΛCDM-based simulations of galaxy evolution, including halo occupation distribution (HOD) models, semi-analytic models (SAMs), and hydrodynamic simulations. We find relatively good agreement within a factor of ~ 2–3, for the total (major+minor) merger fraction f, both between the data and models, and between different models. However, there are nearly two orders of magnitude variation in the predicted major merger rates from different models. This is likely tied to to difficulties faced by models in reproducing the observed number density of galaxies on the mass scales of interest. (3) The average SFR of interacting galaxies is only modestly enhanced compared to non-interacting galaxies over $z \sim 0.24$–0.80, among intermediate mass galaxies. Our results of a modest interaction fraction f and a modest enhancement in SFR from interactions culminate in our finding that strongly interacting systems only account for a small fraction ($< 30\%$) of of the cosmic SFR density over $z \sim 0.24$–0.80 (lookback time ~ 3–7 Gyr). In effect, the behavior of the cosmic SFR density over the last 7 Gyr is predominantly shaped by non-interacting galaxies rather than strongly interacting galaxies.

Subject headings: galaxies: fundamental parameters — galaxies: structure — galaxies: kinematics and dynamics — galaxies: evolution

1. Introduction

Hierarchical Λ cold dark matter (ΛCDM) models provide a successful paradigm for the growth of dark matter on large scales. The evolution of galaxies within ΛCDM cosmogonies depends on the baryonic merger history, the star formation (SF) history, the nature and level of feedback from supernovae and AGN, the redistribution of angular momentum via bars or mergers, and other aspects of the baryonic physics. Empirical constraints on the fate

of the baryonic component are key, therefore, for developing a coherent picture of galaxy evolution. They also provide important tests for semi-analytical models (e.g., Kauffmann et al. 1993; Somerville & Primack 1999; Cole et al. 2000; Benson et al. 2005; Khochfar & Burkert(2005); Hopkins et al. 2007), and cosmological N-body (e.g., Donghia et al. 2008;) and hydrodynamical simulations (e.g., Navarro & Steinmetz 2000; Murali et al. 2002; Governato et al. 2004; Robertson et al. 2004; Maller et al. 2006) of galaxy evolution within ΛCDM cosmogonies. In fact, empirical constraints on the interaction and SF history of baryons can help to resolve several major areas of discord between observations and ΛCDM models of galaxy evolution, such as the angular momentum crisis, the problem of bulgeless and low bulge-to-total (B/T) ratio galaxies (Navarro & Benz 1991; Burkert & D'Onghia 2004; Kautsch et al. 2006; Barazza, Jogee, & Marinova 2007; Weinzirl et al. 2008), and the substructure or missing satellite problem.

The interaction history of galaxies impacts the mass assembly, star formation history, AGN activity, and structural evolution of galaxies. At redshifts $z > 2$, corresponding to lookback times $T_{\rm back} > 10.4$ Gyr[17], observations suggest a large merger frequency of $> 40\%$ among massive galaxies (e.g. Conselice et al. 2003; Patton et al. 2000; Le Fevre et al. 2000). At $z < 1$, the volume sampled and sample size used by earlier studies were small leading to uncertain and conflicting results (Conselice et al. 2003; Lin 2004 ; Patton et al 2002; Casato 2005; dePropis 07). Recent studies based on larger samples have employed different methods to characterize the interaction history of galaxies at $z < 1$. Studies based on Gini-M20 coefficients report a fairly constant fraction ($\sim 7 \pm 0.2$ %) of disturbed galaxies over z$\sim$ 0.2 to 1.2 among bright galaxies (Lotz et al 2008) in the AEGIS survey. Other studies based on close pairs report a major merger frequency of $\sim$ 2% to 10% over z$\sim$ 0.2 to 1.2 (Kartaltepe et al 2008) and $\sim$ 5% for massive galaxies at z$\sim$ 0.4 to 0.8 (Bell et al 2006).

Studies to date have brought important insights but face several limitations. The use of automated parameters, such as CAS asymmetry A and clumpiness parameters or Gini-M20 coefficients, to identify interacting galaxies can fail to pick stages of major or minor interaction where distortions do not dominate the total light contribution (§ 3.4). Comparison with simulations suggest that the CAS criterion ($A > 0.35$ and $A > S$) capture major mergers about 1/3 of the time, while the eye is sensitive to major merger features over twice as long (e.g., Conselice 2006; § 3.4). To complicate matters, automated asymmetry parameters can also capture non-interacting galaxies hosting small-scale asymmetries that are produced by stochastic star formation (§ 3.4). In the case of studies based on close (separation $\sim$ 5 to 30 kpc) pairs, the translation of the pair frequency into a merger rate is non-trivial due to

[17]We assume in this paper a flat cosmology with $\Omega_M = 1 - \Omega_\Lambda = 0.3$ and H_0 =70 km s^{-1} Mpc^{-1}.

several factors. The uncertainties in the photometric redshifts can lead to false pairs caused by chance line-of-sight projection. Secondly, even pairs with members at the same redshift may not be gravitationally bound, and may therefore not evolve into a strong interaction or merger in the future. Thirdly, gravitationally bound pairs captured by this method sample different phases of an interaction depending on the separation and any merger rate inferred depends on the separation, orbital eccentricity, and orbital geometry.

In this paper, we present a complementary study of the frequency and impact of strong galaxy interactions on the SF activity of galaxies over $z \sim 0.24$–0.80 (lookback times of 3–7 Gyr) using *HST* ACS, Combo-17, and Spitzer 24 μm data of ~ 3800 galaxies in the GEMS survey. This study complements existing studies in several ways.

1. We use a large sample of ~ 3800 ($M \geq 1 \times 10^9\ M_\odot$) galaxies and ~ 800 high mass ($M \geq 2.5 \times 10^{10}\ M_\odot$) galaxies for robust number statistics (§ 2). Two independent methods are used to identify strongly interacting galaxies: a tailored visual classification system complemented with spectrophotometric redshifts and stellar masses (§ 3.2), as well as automated CAS asymmetry and clumpiness parameters (§ 3.4). This allows the first systematic comparison to date between CAS-based and visual classification results (§ 4.2). We also try to assess the impact of moderate bandpass shifts and surface brightness dimming (§ 4.1).
2. We set up the visual classification system (§ 3.2) so as to target strong interactions with mass ratio $M1/M2 > 1/10$. While many earlier studies focused on major mergers, it is important to constrain minor mergers as well, since minor mergers dominate the merger rates in LCDM models at $z < 1$.
3. We compare the observed fraction f and inferred merger rate R to a suite of ΛCDM-based simulations of galaxy evolution, including both semi-analytical and hydrodynamic SPH-based simulations (§ 4.4). To our knowledge, such extensive comparisons have not been attempted to date, and are long overdue.
4. In § 4.6 to § 4.7, we investigate the impact of interactions on the average SFR and the total UV+IR SFR density of intermediate-to-high mass ($M \geq 1 \times 10^9\ M_\odot$) galaxies over ~ 0.24–0.80. Our work complements the study of the UV (Wolf et al. 2005) and IR (Bell et al. 2005) luminosity density over a smaller redshift bin ($z \sim 0.65$–0.75).

   The relative SF properties of interacting and non-interacting galaxies over ~ 0.24–0.80. is of particular astrophysical interest, given that the cosmic SFR density is claimed to decline by a factor of 3 to 10 since $z \sim 1$ (e.g., Madau et al. 1996, 1998; Cowie et al. 1996; Flores et al. 1999; Haarrsma et al. 2000). The idea that galaxy interactions enhance the SFR of galaxies and trigger strong nuclear starbursts is well established from observations (e.g. Larson & Tinsley 1978; Joseph & Wright 1985; Kennicutt et al.

1987; Barton et al 2003) and simulations (e.g., Negroponte & White 1983; Hernquist 1989; Barnes & Hernquist 1991, 1996; Mihos & Hernquist 1994, 1996; Barnes 2004; Springel, Di Matteo & Hernquist 2005). However, simulations cannot robustly predict the impact of galaxy interactions on the SF activity of galaxies over the last 7 Gyr, since both the SFR and properties of the remnants in simulations are highly sensitive to the stellar feedback model, the bulge-to-disk (B/D) ratio, the gas mass fractions, and orbital geometry (e.g., Cox et al 2006; di Matteo et al. 2007).

2. Dataset and Sample Selection

This study uses data from the Galaxy Evolution from Morphology and SEDS (GEMS; Rix et al. 2004) survey, which provides high resolution *Hubble Space Telescope (HST)* Advanced Camera for Surveys (ACS) images in the F606W and F850LP filters over an 800 arcmin^2 ($\sim 28' \times 28'$) field centered on the Chandra Deep Field-South (CDF-S). Accurate spectrophotometric redshifts [$\delta_z/(1+z) \sim 0.02$ down to $R_{\rm Vega} = 24$] and spectral energy distributions, based on 5 broad bands ($UBVRI$) and 12 medium band filters, are available from the COMBO-17 project (Wolf et al. 2004). The ACS data reach a limiting 5 σ depth for point sources of 28.3 and 27.1 AB mag in F606W and F850LP, respectively (Rix et al. 2004). The effective point spread function (PSF) in a single F606W image is $\sim 0\farcs07$, corresponding to 260 pc at $z \sim 0.24$ and 520 pc at $z \sim 0.80$. In addition to *HST* ACS imaging, the GEMS field has panchromatic coverage which includes *Spitzer* (Rieke et al. 2004; Papovich et al. 2004) and *Chandra* data

We use stellar masses from Borch et al. (2006). We refer the reader to the latter publication for a detailed description and provide only a brief summary here. Objects were classified as main sequence, stars, white dwarfs, galaxies, and quasars using color indices and their photometric redshifts were estimated using simple dust-reddened single-burst SED templates (Wolf et al. 2004). For galaxies and quasars, the joint probability of a given redshift and a given rest-frame SED is derived and this procedure provides a minimum error variance estimation of both the redshift and the SED template. Once the redshfit has been estimated, the SEDs in 17 bands were fitted with a new set of template SEDs with more plausible SF histories in order to derive a stellar M/L (Borch et al. 2006). The library of SEDs is built using the PEGASE-code and the underlying SF histories are parameterized by the three-component model, with a Kroupa (Kroupa et al. 1993) initial mass function (IMF) adopted in the mass regime 0.1–120 $M_\odot$.

We present the results based on the visual classification and CAS parameters (§ 3) of GEMS F606W, rather than F850LP images, for the following reasons. The F606W im-

ages are $\sim$ 1.2 magnitude deeper than the GEMS F850LP images and allow more reliable characterization of morphological features in the presence of cosmological surface brightness dimming at the rate of $(1+z)^{-4}$ (e.g., Barden et al. 2007). Furthermore, the low signal to noise in the F850LP images leads to large error bars on the asymmetry A and clumpiness S parameters generated by the CAS code, effectively making it impractical to use these values in CAS merger diagnostics (§ 3.4). When using the F606W images, we only include results over the redshift range $z \sim 0.24$–0.80 in order to ensure that the rest-frame wavelength $\lambda_{\rm rest}$ stays primarily in the optical band and does not shift to the far-UV. In the fourth redshift bin ($z \sim 0.6$ to 0.8) $\lambda_{\rm rest}$ shifts to the violet/near-UV (3700 Å to 3290 Å), but as we show in § 4.1, this does not significantly impact the results. We discard the last redshift bin ($z \sim 0.80$–0.95) where $\lambda_{\rm rest}$ shifts into the far-UV. In summary, based on the above considerations, we are left with a sample of $\sim$ 4740 galaxies with $R_{\rm Vega} \leq 24$, over $z \sim 0.24$–0.80 ($T_{\rm back} \sim$ 3–7 Gyr).

Figure 1 shows the rest-frame $U-V$ color plotted versus the stellar mass for this sample of $\sim$ 4740 galaxies. The redshift interval is divided into four 1 Gyr bins. The diagonal line marks the separation of the red sequence and the blue cloud galaxies (BCG) at the average redshift $z_{\rm ave}$ of the bin. We use the definition in Borch et al. (2006) and Bell et al. (2004) for CDF-S:

$$(U-V)_{\rm rest} > 0.227\ \log({\rm M/M_\odot}) - 1.26 - 0.352{\rm z} \qquad (1)$$

The vertical lines on Figure 1 marks the mass completeness limit (Borch et al. 2006) for the red sequence galaxies. The blue cloud galaxies are complete well below this mass.

In this paper, we present further results for two samples of astrophysical interest. The first sample (henceforth sample S1) focuses on galaxies with high stellar mass ($M \geq 2.5\times10^{10}$ $M_\odot$; Table 1). The sample size is originally 804 galaxies, out of which 798 (99.2%) could be visually classified. For this stellar mass range, the red sequence and blue cloud galaxies are both complete out to the highest redshift bin $z \sim 0.62$–0.80 for our sample, and we have theoretical predictions for comparison (see § 4.5) from semi-analytical models (e.g, Somerville et al. 2008; Hopkins et al. 2007; Khochfar & Burkert(2005); Bower et al. 2006), N-body (D'Onghia et al. 2008), and hydrodynamical SPH simulations (e.g., Maller et al. 2006). Note that the survey has few galaxies above 10^{11} $M_\odot$ (Fig. 1), and hence the high mass ($M \geq 2.5 \times 10^{10}$ $M_\odot$) sample primarily involves galaxies in the range 2.5×10^{10} to 10^{11} $M_\odot$.

We also present selected results for the sample S2 of intermediate stellar mass ($M \geq 1 \times 10^9$ $M_\odot$), which consists of 3860 galaxies, of which 3698 or $\sim$ 96% could be visually classified. However, we note that for this mass range, the blue cloud is complete in our sample out to

$z \sim 0.80$, while the red sequence is incomplete in the higher redshift bins. Where appropriate, we will therefore present results for sample S2, as well as for the blue cloud (e.g.,Table 2).

3. Methodology: Identifying Interacting and Non-Interacting Galaxies

3.1. Overview of The Methodology

Galaxy mergers and interactions with mass ratio $M1/M2 > 1/10$ can have a significant impact on galaxy evolution. According to simulations, major mergers (defined as those with mass ratio $1/4 < M1/M2 \leq 1/1$) typically destroy disks, transforming them via violent relaxation, into systems with an $r^{1/4}$ de Vaucouleurs-type stellar profile, such as ellipticals (e.g., Negroponte & White 1983; Barnes & Hernquist 1991; Mihos & Hernquist 96; Struck 1997; Naab & Burkert 2001; but see Robertson et al 2004). These simulations suggest that ongoing/recent major mergers at $z \leq 1$ are associated with arcs, shells, ripples, tidal tails, large tidal debris, extremely asymmetric light distributions, double nuclei inside a common body, galaxies linked via tidal bridges of light, and galaxies enclosed within the same distorted envelope of light.

Minor mergers (defined as those with $1/10 < M1/M2 \leq 1/4$) of two spirals will not destroy the disk of the larger spiral (e.g., Hernquist & Mihos 1995; Smith et al. 1997; Jogee et al. 1999). Typically, the smaller companion sinks via dynamical friction, may excite warps, bars, spirals, and other non-axisymmetric perturbations, and leads to vertical heating, arcs, shells, ripples, tidal tails, tidal debris, warps, offset rings, highly asymmetric light distributions, etc (e.g., Quinn et al. 1993; Hernquist & Mihos 1995; Mihos et al. 1995; Quinn, Hernquist, & Fullagar 1993; Smith et al. 1997; Jogee et al. 1999; review by Jogee 2006 and references therein).

One goal of this paper is to identify strongly interacting systems, which are likely candidates for an ongoing or recent interaction of mass ratio $M1/M2 > 1/10$. As a guide to identifying these systems, we use the afore-mentioned morphological signatures seen in simulations. We employ two methods: a tailored visual classification system (§ 3.2), and quantitative asymmetry (A), and clumpiness (S) parameters (§ 3.4) derived using the CAS code (Conselice et al. 2000). While many studies use only automated methods or visual classification, we choose to use both methods in order to better assess the systematics, and to test the robustness of our results.

To further constrain galaxy evolution, it would be useful if we could separate these strongly interacting systems into major ($1/4 < M1/M2 \leq 1/1$) versus minor ($1/10 < M1/M2 \leq 1/4$) interactions. However, for many strongly interacting galaxies it is not

possible to unambiguously make this distinction, since the morphological disturbances induced depend not only on the mass ratio of the progenitors, but also on the orbital geometry (prograde or retrograde), the gas mass fraction, and structural parameters (e.g., Mihos & Hernquist 96; Struck 1997; Naab & Burkert 2001; Mihos et al. 1995, di Matteo et al. 2007). In effect, many signatures could be caused by both major and minor interactions. Thus, in § 3.3, we divide the strongly interacting systems into three categories: major, minor, and major/minor interactions. The last category includes ambiguous cases that could be either major or minor, while the first two categories are clear cases of major and minor interactions, respectively. They allow us to set lower limits to the major and minor merger fraction.

3.2. Visual Classification of Galaxies as Interacting and Non-Interacting

We visually classified F606W images of the sample of ~ 4740 galaxies (§ 2) with $R_{\rm Vega} \leq 24$ in the redshift range $z \sim 0.24$–0.80. A small subset (below 6%) of galaxies could not be classified due to image defects, low signal to noise, highly compact appearance, etc.

As described in § 3.1, the main goal of this paper is to identify strongly interacting candidates, which are likely candidates for an ongoing or recent interaction of mass ratio $M1/M2 > 1/10$. We use the morphological signatures suggested by the simulations outlined in § 3.1 to identify these systems and assign them the visual class of strongly interacting ('Int') galaxies. Figure 2 shows examples in the four 1 Gyr redshift bins. In practice, the class 'Int' of interacting galaxies consists of two sub-groups, 'Int-1' and 'Int-2', described below.

1. 'Int-1': A galaxy is assigned an 'Int-1' class if it exhibits a *strong morphological distortion*, such as a warped disk, an offset ring, arcs, shells and ripples, tidal tails, large tidal debris, extremely asymmetric light distributions, double nuclei inside a common body, and tidally distorted bridges of light. The basic idea here is that 'Int-1' galaxies are unambiguous cases of strongly interacting galaxies, since they exhibit the *morphological distortions induced by a strong gravitational disturbance*. The class 'Int-1' is independent of the accuracy of the spectrophotometric redshift. Examples of 'Int-1' interacting systems are shown as cases 3, 4, 5, 6, 7, 8, 9, 10, 11, and 12.
2. 'Int-2': A galaxy is assigned an 'Int-2' class if it is *fairly symmetric*, but has a companion, which satisfies four criteria: it is overlapping or in contact with it so that the two galaxies share a common envelope of light, making the pair be effectively a 'contact pair'; it is within a projected separation d of less than 20 kpc; it has the same Combo-17 spectrophotometric redshift within the accuracy $\delta_z/(1+z) \sim 0.02$ (§ 2); its stellar mass ratio satisfies $M1/M2 > 1/10$. The classification of a galaxy as an Int-2 contact

pair depends on the accuracy of the spectrophotometric redshift, but 'Int-2' contact pairs are less likely to be be line-of-sight chance projection than more distant pairs with $d \sim 20$ to 30 kpc. Examples of 'Int-2 interacting systems include both galaxies in case 7 of Fig 5, and the lower fairly symmetric galaxy in case 1 of Fig. 2. Most of our interacting systems fall in the class 'Int-1' rather than 'Int-2'.

Galaxies that show no evidence of an ongoing or recent interaction of mass ratio $> 1/10$, according to the above-established criteria, are classified as 'Non-Interacting' galaxies. These galaxies may harbor very subtle distortions, but none of the type described in 'Int-1 and 'Int-2'. Galaxies in the class of 'Non-Interacting' consists of two sub-groups, 'Non-Interacting E-to-Sd' and 'Non-Interacting Irr1', which are shown in Figure 3, and described below.

1. 'Non-Interacting Irr1': It is important to note that even non-interacting galaxies have some inherent level of small-scale asymmetries in optical light due to SF activity. In the case of low mass galaxies, further asymmetries may also arise due to the low ratio of rotational to random velocities, as is commonly seen in Im and Sm. These internally-triggered asymmetries due to SF in non-interacting galaxies differ in scale (few 100 pc vs several kpc) and morphology from the externally-triggered distortions typical of the 'Int-1' class. We classify non-interacting galaxies with such internally-triggered asymmetries as 'Irr1' (see Figure 3). Such systems may get accidentally picked as 'interacting' in automated asymmetry-based codes (see § 4.2).
2. 'Non-Interacting E-to-Sd': Galaxies are assigned the 'E to Sd' class if they are fairly symmetric, have Hubble types in the range E-to-Sd, and are not associated with any overlapping or contact companion.

In this paper, we are primarily concerned about the differences between three groups: the strongly interacting galaxies in class 'Int', the 'ion-interacting E-to-Sd' galaxies, and the 'non-interacting Irr1' galaxies. The details of how 'E-to-Sd' galaxies are further sub-divided into individual Hubble types do not have any major impact on our main results, and we only describe this sub-classification for the sake of completeness. In the Hubble classification system (1936), as we go from E to Sd, the bulge to disk (B/D) luminosity ratio, as well as smoothness and tightness of any spiral arms, are expected to decrease. The Hubble system works fairly well on average in field galaxies, although it may fail in clusters (e.g., Koopmann & Kenney 1998). We use conventional definitions (Binney & Merrifield 1998) for individual Hubble types (E, S0, Sa, Sb-Sc, and Sd). We assign an elliptical (E) type if a galaxy exhibits a smooth featureless appearance, show no disk signatures, such as a bar or spiral arms, and appear to be pure spheroids. We assign an S0 class if a galaxy hosts a smooth central brightness condensation, surrounded by an outer component, which is relatively featureless

(without spiral arms) and has a less steeply declining brightness profile (Binney & Merrifield 1998). We assign Sa, Sb-Sc, and Sd types using primarily visual estimates of the B/D ratio, and secondarily the smoothness/clumpiness of the disk. We do not accord much weight to the smoothness of spiral arms since the ACS F606W PSF ($\sim$ 260–560 pc at $z \sim 0.24$–0.80) precludes the identification of fine structures in the arms. In fact, at intermediate redshifts, where the faint smooth arms of Sa galaxies are not easily discernible, the distinction between E, S0, and Sa becomes blurred (see also § 4.1). However, this ambiguity between Es, S0s and Sas is not a problem for the subsequent analyses in this paper, since galaxies are grouped together either as 'E+S0+Sa' or 'E-to-Sd'.

The fractions of interacting, 'non-interacting E-to-Sd' galaxies, and ' non-interacting Irr1' galaxies. are shown in Table 1 for the high mass sample, and in Table 2 for the intermediate mass sample. Further results and tests on the interaction history from visual classes are presented in § 4.1.

3.3. Separating interacting galaxies into major and minor interactions

There are numerous astrophysical questions for which it would be useful to know which of the interacting systems are major ($M1/M2 \geq 1/4$) versus minor ($1/10 \leq M1/M2 < 1/4$) interactions. However, the morphological distortions induced in an interaction depend not only on the mass ratio $M1/M2$ of the progenitors, but also on the orbital geometry (prograde or retrograde), the gas mass fraction, and structural parameters (e.g., Mihos & Hernquist 96; Struck 1997; Naab & Burkert 2001; Mihos et al. 1995, di Matteo et al. 2007). For instance, both types of mergers can cause strong tidal disturbances, drive large gas inflows into the inner kpc and trigger intense starbursts or AGN activity (e.g, review by Jogee 2006 and references therein). Furthermore, prograde mergers occur faster than retrograde mergers, lead to more violent disruption, and excite larger non-circular motions (e.g., Binney & Tremaine 1987).

Therefore, we divide the strongly interacting systems into three categories: major, minor, and major/minor interactions. The first (second) category consists of fairly unambiguous cases of major (minor) interaction, with unique morphological tell-tale signatures. The last category of 'major or minor interaction' includes ambiguous cases, where the morphological distortions and visual appearance could be due to either a major or a minor interaction.

The 'major or minor interaction' category includes the following cases: a) Galaxies with double nuclei that are asymmetrically located, have different luminosities, and whose mass ratio is unknown as the system has only one single stellar mass based on COMBO-17 data

(e.g., case 8 in Fig. 2). b) Systems with a morphological distortion that is strong, but not a 'train-wreck' (e.g., cases 3, 4, 5, 6, 7, 10, 11 in Fig. 2).

We assign a class of 'minor interaction' to the following cases: (a) We consider galaxies that have undergone a recent interaction, but still host an extended disk to be a case minor merger, since such mergers do not destroy disks. We include in this group isolated galaxies that harbor a warped disk (e.g., case 2 in Fig. 2) or isolated strongly distorted disk with tidal debris and tails (e.g., cases 9 in Fig. 2). (b) We include galaxies (see § 3.2) with a companion that satisfies three criteria: it is overlapping or in contact so that the two galaxies share a common envelope of light; it has the same Combo-17 spectrophotometric redshift within the accuracy $\delta_z/(1+z) \sim 0.02$ (§ 2); and its stellar mass ratio satisfies $(1/10 \leq M1/M2 < 1/4)$. Such minor mergers are in progress (e.g., case 2, 4 in Fig. 2).

We assign a class of 'major interaction' to the following cases: (a) Galaxies with extremely distorted 'train-wreck' morphologies. (b) Galaxies with double nuclei that are symmetrically located and have comparable luminosities (e.g., case 6, 12 in Fig. 2). (c) Galaxies with a companion that satisfies three criteria: it is overlapping or in contact so that the two galaxies share a common envelope of light; it has the same Combo-17 spectrophotometric redshift within the accuracy $\delta_z/(1+z) \sim 0.02$ (§ 2); and its stellar mass ratio satisfies $(M1/M2 > 1/4)$. Such major mergers are in progress (e.g., cases 1 with a stellar mass ratio $\sim 1/4$ in Fig. 2; case 7 with a stellar mass ratio of ~ 0.5 in Fig 5).

The fraction of interacting galaxies, and their subdivision into the classes 'minor interaction', 'major interaction', and 'major or minor interaction' are shown in Table 1 for the high mass sample, and in Table 2 for the intermediate mass sample. The results are further discussed in § 4.3.

3.4. CAS

We derived the concentration C, asymmetry A, and clumpiness S (CAS) parameters by running the the CAS code (Conselice et al. 2000) on the F606W images. As is standard practice, the segmentation maps produced during the original source extraction (Caldwell et al. 2006) are used to mask neighbors on each ACS tile. The CAS code derives the asymmetry index A (Conselice 2003a) by rotating a galaxy image by 180 deg, subtracting the rotated image from the original image, summing the absolute intensities of the residuals, and normalizing the sum to the original galaxy flux. CAS improves the initial input center with the IRAF task 'imcenter' and then performs a further refinement within a 3×3 grid, picking the center that minimizes A. The CAS concentration index C (Bershady et al. 2000)

is proportional to the logarithm of the ratio of the 80% to 20% curve of growth radii within 1.5 times the Petrosian inverted radius at $r(\eta = 0.2)$, normalized by a logarithm

$$C = 5 \times \log(\mathrm{r_{80\%}}/\mathrm{r_{20\%}}) \tag{2}$$

The clumpiness index S (Conselice 2003) is defined as the ratio of the amount of light contained in high-frequency structures to the total amount of light in the galaxy. In order to compute S, the CAS code first smooths the galaxy image, to produce a lower resolution image whose high-frequency structure has been washed out. The latter image is then subtracted from the original image to produce a residual map that contains only the high-frequency components of the galaxy's stellar light. The flux of this residual light is then summed and divided by the sum of the original galaxy image flux to obtain a galaxy's clumpiness (S) value. Tests on the interaction history from CAS are presented in § 4.2.

It has been argued that the criterion $A > 0.35$ and $A > S$ (henceforth referred to as the CAS merger/interaction criterion) captures galaxies that exhibit large asymmetries produced by strong interactions (Conselice 2003a) . We will assess this in § 4.2.

4. Results and Discussion

4.1. The interaction fraction from visual classes

Fig 4 compares the fraction (f) of strongly interacting galaxies, for both high mass ($M \geq 2.5 \times 10^{10}\ M_{\odot}$) and intermediate mass ($M \geq 1 \times 10^{9}\ M_{\odot}$) sample, based on visual classification by 3 classifiers (SJ, SM, KP). On this figure, the plotted error bar for f only includes the binomial term $[f(1\text{-}f)/N)]^{1/2}$, for each bin of size N. The same trend is seen for all 3 classifiers and the maximum spread δ_{f}/f in the 4 bins is 15%, 17%, 26% and 26%, respectively. In subsequent analyses, we adopt an error bar on f that includes in quadrature both the binomial term and a dispersion of 26% to capture the inherent subjectivity in the visual classification.

Another key test is to assess the impact of redshift-dependent systematic effects, such as bandpass shifting. When using the F606W filter whose pivot wavelength is ~ 5915 Å, the rest frame wavelength (λ_{rest}) corresponds to the rest-frame optical at the mean redshift of the first 3 bins, but shifts to the rest-frame violet/near-UV (3700 Å to 3290 Å) in the last bin ($z \sim 0.6$ to 0.8). Galaxies tend to look slightly more asymmetric at near-UV wavelengths due to the prominence of young stars. In order to quantitatively test the impact of bandpass shift on our visual classes, we use the redder F850LP images from the GOODS survey,

which overlaps with the central 20% of the GEMS survey area. The F850LP filter has a pivot wavelength of 9103 Å and traces the rest-frame optical (7340 Å to 5057 Å) in all four redshift bins out to $z \sim 0.8$. They also have 5 times longer exposures than the GEMS F850LP and F606W images. Fig 5 shows GEMS F606W and GOODS F850LP images of typical disturbed and normal galaxies in the last 2 redshift bins ($z \sim 0.47$ to 0.8).

While the GOODS images have higher S/N, and trace redder older stars, they do not reveal dramatically different morphologies from from those in the GEMS F606W images (Fig 5). Furthermore, the 855 intermediate mass ($M \geq 1 \times 10^9\ M_{\odot}$) galaxies in the GEMS/GOODS overlap area, were classified using both GOODS F850LP and GEMS F606W images by the 3 classifiers. We find that the ratio of ($f_{\rm GEMS}/f_{\rm GOODS}$) ranges from 0.8 to 1.2 across the 3 classifiers (Table 3), where $f_{\rm GEMS}$ and $f_{\rm GOODS}$ are the fraction of strongly interacting galaxies based on the GEMS F606W and GOODS F850LP images, respectively.The mean f changes by only 6% (Table 3). In effect, over 85% of the galaxies classified as disturbed ('Int') in the GEMS F606W images retain the same visual class in the GOODS F850LP. Among the remaining objects, some classified as 'Non-Interacting' in GEMS F606W get reclassified as disturbed in GOODS F850LP, and vice-versa The fact that f does not change by a large amount between GEMS F606W and GOODS F850LP is not surprising, since the rest-frame wavelength of GEMS F606W in the last bin shifts only to the violet/near-UV, rather than to the far-UV, where morphological changes are more dramatic. We conclude that our results are not highly impacted by bandpass shifting, and any effect is accounted for by our error bars of $> 26\%$ in f.

Another redshift-dependent systematic effect is surface brightness dimming at the rate of $(1+z)^{-4}$ (e.g., Barden et al. 2008). This leads to surface brightness dimming by a factor of 1.0 to 2.5 magnitude over the redshift range 0.24 to 0.80. This is mitigated in part by two factors: galaxies are on average 1.0 magnitude brighter in surface brightness by $z \sim 0.8$ (e.g., Barden et al. 2005), and the average SFR rises by a factor of ~ 4 out to $z \sim 0.8$ (e.g., see § 4.6). Two approaches can be adopted to assess the impact of surface brightness dimming. The first is to artificially redshift strongly disturbed galaxies in the lowest redshift bin ($z \sim 0.24$) out to $z \sim 0.8$, either assuming passive evolution or adding in a ~ 1 magnitude of brightening in surface brightness. However, this approach suffers from the limitation that it implicitly assumes that galaxies at $z \sim 0.8$ are similar to those at $z \sim 0.24$ and evolve passively with time. A better approach, which does not make such assumptions, is to repeat the analysis and visual classification using *deeper* images of the galaxies and assess the resulting change in visual classes. The above-described test performed using the deep GOODS F850LP image (Fig. 5) is an example of such a test.

Finally, as an extra test, we checked the distribution of Sérsic indices n for single-

component Sérsic fits (Barden et al. 2005) for the visual classes of the sample S2 of intermediate mass $M \geq 1 \times 10^9\ M_\odot$ (Fig. 6). Non-interacting disk-dominated systems are expected to have $n < 2.5$, while massive ellipticals and bulge-dominated systems typically have higher Sérsic indices. We indeed find that over 85% of the systems visually classified as Sb-Sd and Irr have $n < 2.5$ in the intermediate mass ($M \geq 1 \times 10^9\ M_\odot$) sample. The systems typed as ellipticals (E) have mostly $n > 3$, and as expected, their distribution peaks at $n \sim 4$, corresponding to a de Vaucouleurs profile. The S0 and Sa types have n values bridging those of the E and disk (Sb-Sc and Sd-Irr) systems. Most of them have $n < 3$, but there is a long tail of S0s and Sas with higher n. This is expected given the previously described (§ 3.2) difficulties in separating E, S0, and Sa galaxies at intermediate redshifts. However, this ambiguity between Es, S0s and Sas is not a problem for the subsequent analyses in this paper, since galaxies are grouped together either as 'E+S0+Sa' or 'E-to-Sd'. In fact, as stressed in § 3.2, the main results presented in this paper depend only on the differences between three groups: strongly interacting galaxies ('Int'),'Non-Interacting E to Sd', and 'Non-Interacting Irr1'.

4.2. The interaction fraction from CAS

In numerous published studies, the CAS merger criterion ($A > 0.35$ and $A > S$) is widely used, in a blind automated mode, to identify strongly interacting galaxies. However, few systematic studies have been done of the potential caveats, which include the following: a) The CAS criterion ($A > 0.35$ and $A > S$) will miss out strongly interacting galaxies where the morphological distortions contribute to more than 35 % of the total galaxy flux. (b) Calibrations of A with N-body simulations (Conselice 2006) shows that during major mergers with mass ratios 1:1 to 1:3, the asymmetry oscillates with time. Typically, it exceeds 0.35 for $\sim$ 0.2 Gyr in the early phases when the galaxies start to interact, falls to low values as the galaxies separate, rises for $\sim$ 0.2 Gyr as they approach again for the final merger, and eventually tapers down as the final remnant relaxes. On average, the $A > 0.35$ criterion is only satisfied for one third of the merger timescale in these N-body simulations. For minor mergers of mass ratios 1:5 and below, the asymmetries are too low to satisfy $A > 0.35$. (c) To complicate matters, automated asymmetry parameters can also capture non-interacting galaxies whose visible light shows small-scale asymmetries due to star formation (e.g., Miller et al. 2008)

In this paper, we perform the first systematic comparison to date between CAS-based and visual classification results and assess the effectiveness of the CAS merger criterion ($A > 0.35$ and $A > S$), for both high mass ($M \geq 2.5 \times 10^{10}\ M_\odot$) and intermediate mass

($M \geq 1 \times 10^9\ M_\odot$) galaxies.

Fig 4 compares the interaction fractions that would be obtained using the CAS criterion ($f_{\rm CAS}$), as opposed to visual classification (f). For the high mass ($M \geq 2.5 \times 10^{10}\ M_\odot$) galaxies, visually based and CAS-based interaction fractions agree within a factor of two, with f being higher than $f_{\rm CAS}$) at $z < 0.5$ and lower at $z > 0.5$ (top panel of Fig 4) However, for the intermediate mass ($M \geq 1 \times 10^9\ M_\odot$) galaxies (lower panel of Fig 4), at $z > 0.5$ the CAS-based interaction fraction can be systematically higher by a factor ~ 3 than the visually based f. The reason for this discrepancy, as we show below, is that at bluer rest-frame wavelengths the CAS criterion picks up a significant number of non-interacting dusty, star-forming galaxies.

Fig. 7 plots the CAS asymmetry A and clumpiness S parameter for galaxies in the four bins covering the redshift interval $z \sim 0.24$–0.80. Galaxies satisfying the CAS criterion ($A > 0.35$ and $A > S$) lie in the upper left hand corner, bracketed by the $A = S$ and $A = 0.35$ lines. One can see that while the CAS criterion captures a fair fraction of the strongly interacting galaxies (coded as orange stars), it also picks up a large number of non-interacting galaxies.

This is further illustrated in Fig. 8. The top panel show the recovery fraction of CAS, defined as the fraction of the visually-classified strongly interacting galaxies ('Int') picked up by the CAS criterion ($A > 0.35$ and $A > S$). For the intermediate mass ($M \geq 1 \times 10^9\ M_\odot$) sample, the CAS criterion picks up only 40% to 50% of the galaxies visually typed as strongly interacting ('Int'). We inspected the systems missed out by the CAS criterion ($A > 0.35$ and $A > S$) and show typical cases in the top panel of Fig. 9. The missed cases include kinematic pairs of relatively symmetric galaxies (e.g., case 1 in Fig. 9); galaxies where the tidal features and small accreted satellite in the main disk of a galaxy (e.g., case 3 in Fig. 9) likely contribute less than 35% of the total light; and galaxies with close double nuclei (e.g., case 2 in Fig. 9), where CAS might refine the center to be between the two nuclei, thereby leading to a low $A < 0.35$.

The lower panel of Fig. 8 illustrates the contamination level of the CAS system. $N_{\rm CAS}$ represents the number of systems picked up by the CAS criterion ($A > 0.35$ and $A > S$) in the four redshift bins. The vast majority (65% to 85%) of these systems turn out to be 'Non-Interacting Irr1' galaxies, and 'Non-Interacting Sb-Sd'. Typical cases are shown in the lower panel of Fig. 9. They include non-interacting actively star-forming systems where SF induces small-scale asymmetries in the optical blue light (e.g., cases 4 and 6 in Fig. 9); systems where A is high due to the absence of a clearly defined center (e.g., case 8 in Fig. 9) or due to the center being blocked by dust (e.g., cases 4 and 9 in Fig. 9); galaxies whose outer parts look irregular (e.g., cases 7 and 8 in Fig. 9); and edge-on systems and compact

systems, where the light profile is steep such that small centering inaccuracies can lead to large A (e.g., case 9 in Fig. 9).

Thus, in summary we conclude that the CAS-based interaction fraction agrees within a factor of two with visually based one for high mass ($M \geq 2.5 \times 10^{10}$ $M_{\odot}$) galaxies, but can overestimate the interaction fraction at $z > 0.5$ by a factor ~ 3 for intermediate mass ($M \geq 1{\times}10^{9}$ $M_{\odot}$) galaxies. For the latter mass range, the systems counting toward $f_{\rm CAS}$ are a mixed bag: the CAS criterion misses about half of the visually-classified strongly interacting galaxies, but picks up a significant number of non-interacting dusty, star-forming galaxies. This contamination will affect the integrated properties of interacting systems captured by CAS and these caveats must be borne in mind in studies that use CAS in blind automated mode.

4.3. Interaction history of massive galaxies

Based on the tests in § 4.1 and § 4.2, we decide to adopt the mean interaction fraction f based on visual classes.. The fraction of interacting galaxies as a function of redshift over the last 7 Gyr is shown in Table 1 for the high mass sample, and in Table 2 for the intermediate mass sample. The error bar shown on f now includes the sum in quadrature of a binomial term $[f(1\text{-}f)/N)]^{1/2}$ for each bin of size N, along with a fractional error of $\pm$ 26% to capture the dispersion between classifiers, and uncertainties due to bandpass shifting and surface brightness dimming.

From Table 1 and Fig. 11, it can be seen that the fraction f of strongly interacting systems among high mass ($M \geq 2.5{\times}10^{10}$ $M_{\odot}$) galaxies remains fairly constant over lookback times of 3–7 Gyr, ranging from 9% $\pm$ 5% at $z \sim 0.24$–0.34, to 8% $\pm$ 2% at $z \sim 0.60$–0.80, as averaged over every Gyr bin. As discussed in § 3.1, these systems are candidates for a recent/ongoing interaction of mass ratio $M1/M2 > 1/10$.

The division of the interaction fraction between 'minor interaction', 'major interaction', and 'major or minor interaction' (§ 3.3) is shown in Table 1 for the high mass sample. The lower limit on the major ($M1/M2 > 1/4$) merger/interaction fraction ranges from 1.1% $\pm$ 0.1% to 3.5% $\pm$ 2.2% over $z \sim 0.24$–0.80. The corresponding lower limit on the minor ($1/10 \leq M1/M2 < 1/4$) interaction fraction ranges from 3.6% $\pm$ 2.2% to 7.5% $\pm$ 2.7%. The interacting galaxies could be either major or minor mergers and make up a fraction between 1.2% to 2.0%. To our knowledge, this is the first, albeit approximate, empirical estimate of the frequency of minor mergers over the last 7 Gyr, since $z \sim 0.80$. It provides an important constraint since minor mergers dominate the merger rates in LCDM models at $z < 1$.

When converting the observed fraction f of interacting galaxies into an interaction rate R, we must bear in mind that in any observational search for galaxy interactions, mergers can only be recognized for a finite time $t_{\rm vis}$, which is the timescale over which an interacting galaxy will appear morphologically distorted. This timescale depends on the mass ratio of the interaction as well as the gas fraction of the progenitors: $t_{\rm vis} \sim 0.5$ 0.8 for gas-rich galaxies, and $t_{\rm vis} \sim 0.2$–0.4 Gyr for gas-poor galaxies (T.J. Cox, private communication). This timescale will also depend on many observational factors such as the method used to identify mergers (e.g. visual classification vs. CAS or other statistical methods) and the depth of the imaging used. We assume a representative value of $t_{\rm vis} = 0.5$ Gyr here, but we must keep in mind that there are at least factors of two uncertainty in this number. The interaction rate R is given by

$$R = \frac{n\ f}{t_{\rm vis}} \tag{3}$$

where n is the comoving number density of galaxies in the redshift bin. For our measured interaction fraction and assumed value of $t_{\rm vis} \sim 0.5$ Gyr, the corresponding interaction rate R is a few $\times 10^{-4}$ galaxies Gyr^{-1} Mpc^{-3} (Fig. 12). It also follows that the number of interactions of mass ratio $> 1/10$ undergone by each massive galaxy is $f/t_{\rm vis} \sim 0.18$ per Gyr, or ~ 0.7 over the redshift interval $z \sim 0.24$–0.80 ($T_{\rm back} \sim 3$–7 Gyr). *Of these 0.70 interactions, which each massive galaxy has undergone since $z \sim 0.8$, we estimate that 0.19 are major mergers, 0.44 are minor mergers and the rest are either major or minor mergers.*

For the intermediate mass ($M \geq 1 \times 10^9\ M_\odot$) sample, we are only complete for blue cloud galaxies. The blue cloud interaction fraction is quite similar to the one for the high mass sample, and ranges from 15% ± 5% to 7% ± 2% over $z \sim 0.24$–0.80 (Table 2. The corresponding interaction rate R ranges from 8×10^{-4} to 1×10^{-3} galaxies Gyr^{-1} Mpc^{-3} .

4.4. Comparison with other studies

When comparing our observed fraction f of strongly interacting galaxies in the high mass ($M \geq 2.5 \times 10^{10}\ M_\odot$) sample over $z \sim 0.24$–0.80 with published studies, several caveats must be borne in mind. Many studies have small samples and large error bars at $z < 0.8$ (e.g., Conselice 2003; Fig. 10). Others focus on bright galaxies and luminosity-selected samples (e.g., Lotz et al. 2008; Casato et al. 2005) rather than stellar mass selected sample, because the data to derive stellar masses were unavailable. Different studies target different systems, ranging from morphologically distorted galaxies to close pairs with separation $d \sim 5$ to 30 kpc. Finally, most studies focus only on major interactions, while the strongly interacting galaxies identified in our study are candidates for a recent/ongoing interaction of mass ratio

$M1/M2 > 1/10$ (§ 3.1), and include both minor and major interactions. Nonetheless, we attempt approximate comparisons.

Fig. 10 shows the the fraction $f_{\rm Gini}$ of morphologically disturbed systems based on Gini-M20 parameters among $M_{\rm B} <$ -20.5 and $L_{\rm B} > 0.4\ L_*$ galaxies in the Extended Groth Strip (Lotz et al. (2008). The latter study does not present any results for a high mass sample, and thus we effectively are comparing their bright galaxies to our high mass galaxies. Over $z \sim$0.2–0.80, our results are in very good agreement, within a factor of less than two, with $f_{\rm Gini}$. The CAS-based results from Conselice (2003) are derived from a small sample in the Hubble Deep Field and have error bars that are too large to set useful constraints at $z < 1$ (Fig. 10).

The major merger fraction of massive galaxies ($M_* \geq 2.5{\times}10^{10}\ M_\odot$) in close ($d < 30$ kpc) pairs based on the 2-point correlation function, is 5% ± 1% averaged over at $0.4 < z < 0.8$ (Bell et al. 2007). The study of luminous ($L_{\rm V} > 0.4\ L_*$) pairs at projected separations of 5–20 kpc in the COSMOS field (Kartaltepe et al. 2007) finds a galaxy pair fraction of $\sim$ 1%–3% over $z \sim$ 0.24–0.80, corresponding to a galaxy merger fraction of $\sim$ 2%–6% (Fig. 10). Our observed fraction f of $\sim$ 6% to 12% over $z \sim$ 0.24–0.8, and our lower limit on the major merger fraction ($f_{\rm major} \geq 2.5\%$) bracket these results. The merger fraction based on close pairs seems to more closely trace the major merger fraction $f_{\rm major}$ from our studies, rather than the total f, as might be expected. However, one should note the following caveats in this comparison. The merger fraction based on close pairs depends on the correction applied to the projected close pair fraction to account for contamination from false pairs caused by chance line-of-sight projection. The correction is model-dependent and depends on the detailed form of the correlation function and uncertainties in the photometric redshifts (e.g., Bell et al. 2007; Kartaltepe et al. 2007). Furthermore, even pairs with members at the same redshift may not be gravitationally bound, and may therefore not evolve into a strong interaction or merger in the future. These factors may cause this method to overestimate the major merger fraction. Another complication when comparing pair-based fraction to our results is that strongly interacting galaxies (as defined in § 3.2) trace a later phase of interaction than the early pre-merger phases traced by close pairs.

4.5. Comparison of interaction history with LCDM simulations

We compare our observed merger fraction f and merger rate R to those predicted by a suite of different theoretical models of galaxy evolution in the context of LCDM cosmology (Fig. 11 and Fig. 12). We first describe the approaches used by the different models.

Predicting the rate of mergers per comoving volume and per unit time between *isolated* dark matter halos within a ΛCDM model is relatively straightforward, and a number of studies of halo interaction rates based on high-resolution N-body simulations have been presented in the literature (refs). However, making a direct comparison with *galaxy* interaction rates is more complicated. When a dark matter halo containing a galaxy merges with a larger halo, the dense core of the halo and the galaxy will continue to orbit within the larger halo for several to several tens of dynamical times, depending on the ratio of the mass of the merging satellite to that of the host halo, and the energy and angular momentum of the orbit. As the sub-halo orbits, it is tidally heated and stripped by the background dark matter, as well as possibly by impulsive encounters with other orbiting satellites. Many small mass or low density satellites may be completely destroyed before they actually "merge" with the central galaxy (refs). Even relatively high resolution cosmological N-body simulations typically do not have adequate resolution to track this process in detail, and often satellites are "lost" before they merge because their mass drops below the resolution limit required to identify a (sub)halo. Also, the presence of a dense core of baryons may make merging satellites more robust to tidal destruction, but this effect is not accounted for in cosmological dissipationless N-body simulations.

A further problem is that it is now well known that the correlation between dark halo (or sub-halo) mass and galaxy mass or luminosity is complex and highly non-linear (refs – van den bosch, yang?). Therefore any attempt to extract a *galaxy* merger rate from ΛCDM simulations also must attempt to model the relationship between dark matter and galaxy properties. The three main methods for making this connection are halo occupation distribution (HOD) models, semi-analytic models (SAMs), and hydrodynamic simulations.

A HOD model specifies the probability that a DM halo of a given mass M harbors N galaxies above a given mass or luminosity. The parameters of this function are determined by requiring that statistical observed quantities, such as galaxy mass or luminosity functions and galaxy correlation functions, be reproduced. We consider here the models of Hopkins et al. (2007), in which DM halos are populated with galaxies following a standard HOD approach, and the merger rate of these galaxies within their host halos is calculated via standard or modified dynamical friction formulae. Some of the modified formulae include a gravitational capture cross section, allow for stripping of halos or calibration with N-body simulations. Depending on the models adopted for sub-halo structure and mass functions, the halo occupation statistics, and the dynamical friction formulae used, the model predictions can vary by a factor of order two.

In SAMS, approximate or simplified treatments are used to model cooling of gas, star formation, supernova feedback, and more recently, AGN feedback (e.g., Somerville et al. 2008;

Bower et al. 2006; Croton et al. 2006; Benson et al. 2005; Somerville & Primack 1999; Cole et al. 2000). These models are based within merger trees, which represent the merger history of the isolated DM halos, and are either extracted from cosmological dissipationless simulations or constructed using analytic methods. In some cases, the information on the merging of "sub-structure", i.e., halos that have already merged with a parent halo, is provided by the N-body simulation. In others, when fully analytic merger trees are being used or the simulation does not have adequate resolution, analytic methods must be used to estimate the time for satellite galaxies to merge. In modern SAMs, these recipes are based on well-calibrated modified versions of the Chandrasekhar dynamical friction approximation (e.g. Boylan-Kolchin et al. 2008). The free parameters representing our ignorance about physical processes such as star formation, supernova feedback, and AGN feedback are normalized in order to reproduce observations of nearby galaxies, such as the $z = 0$ galaxy mass or luminosity function. Here we compare our results with three independent SAMs: Somerville et al. (2008), Bower et al. (2006), and Khochfar & Silk (2006).

The SAMs of Khochfar & Silk (2006) calculate dark matter histories based on merger trees proposed in Somerville & Kolatt(1999) with a mass resolution of 5×10^{10} $M_{\odot}$. In an earlier paper Khochfar & Burkert(2001) could show that a simple toy model for the merging history of galaxies based on these dark matter merger trees yields reasonable good agreement with observed merger rates. The baryonic physics within the dark matter halos is calculated from the following recipes presented in Khochfar & Burkert(2005).

Cosmological hydrodynamic simulations attempt to model the detailed physics of gas hydrodynamics and cooling as well as gravity by explicitly solving the relevant equations for particles or grid cells (e.g., Maller et al. 2006; Navarro & Steinmetz 2000; more refs). Smoothed Particle Hydrodynamics (SPH) methods are most commonly used for cosmological simulations. Star formation and supernova feedback is treated using empirical recipes similar to those implemented in semi-analytic models. A drawback of this approach is that, due to computational limitations, state-of-the-art simulations still do not have the dynamic range to resolve the internal structure of galaxies while simultaneously treating representative cosmological volumes. As well, these methods have thus far not been very successful at reproducing basic observed properties of galaxies, such as the internal size and angular momentum content of disks, and the mass or luminosity function of galaxies. This may be in part because most such simulations do not yet include AGN feedback, which is now believed to play a key role in shaping galaxy properties. Here, we show results from the smoothed particle hydrodynamics (SPH) cosmological simulations analyzed by Maller et al. (2006). The simulation box is $22.2h^{-1}$Mpc on a side, and has a spatial resolution of 5 h^{-1}kpc, with the dark matter and gas components modeled with $(128)^3$ particles each. No AGN feedback is included.

We must also consider carefully how merger rates are determined in these simulations. Typically, simulation outputs ("snapshots") are stored at a sequence of redshifts. Upon analyzing these snapshots, one notices that $N_{\rm mrg}$ galaxies that had not merged in a previous lookback time $t_{\rm hi}$ have merged by a later time $t_{\rm lo}$, where the snapshots are separated by a time $\Delta t = t_{\rm lo} - t_{\rm hi}$. The merger rate is then $R = N_{\rm mrg}/(\Delta t V)$, where V is the comoving volume of the simulation box, and the merger fraction is $f = N_{\rm mrg}/N_{\rm gal}$, where $N_{\rm gal}$ is the total number of galaxies above the relevant mass limit. This is the approach that has typically been used in previous studies of merger rates in cosmological simulations.

When comparing the simulations to the observations in a given redshift bin defined by lookback times $t_{\rm hi}$ and $t_{\rm lo}$, all the mergers that occurred within the interval $t_{\rm lo}$ and $t_{\rm hi}+t_{\rm vis}$ are counted in the simulations because such mergers will appear as a morphologically distorted galaxy within the observed redshift window. Here $t_{\rm vis}$ is the visibility timescale defined in § 4.3. The interaction rate is then computed as $R = N_{\rm mrg}/((\Delta t + t_{\rm vis})V)$. For the redshift bins used in our studies, $(\Delta t = t_{\rm lo} - t_{\rm hi}) \sim 1$ Gyr (Table 1). This approach was used in the SAMS of Bower et al. (2006), and Khochfar & Silk (2006), which we present in Fig. 11 and Fig. 12. They adopted a nominal $t_{\rm vis} \sim 0.3$ Gyr. The results based on simulation outputs are not very sensitive to $t_{\rm vis}$ as long as $(\Delta t = t_{\rm lo} - t_{\rm hi}) \gg t_{\rm vis}$.

For the Somerville et al. (2008) models, the simulation analysis was carried out in a way that in closer to the observations. We construct a light cone with a geometry that is equivalent to three GEMS fields (2700 arcmin^2 from $0.1 < z < 1.1$). We then divide the galaxies into redshift bins, as in the observational analysis, and count the number of galaxies that have had a merger within a time $t_{\rm vis}$ in the past. This method of deriving the merger rate and fraction f from a mock catalog is quite sensitive to $t_{\rm vis}$ and can vary by a factor of order two as $t_{\rm vis}$ is varied from 0.3 to 0.5 Gyr.

We compare our observed merger fraction f and merger rate R to those predicted by the theoretical models summarized above in Fig. 11 and Fig. 12. The models were provided to us directly by the authors or co-authors of these individual studies. For the SAMS (Somerville et al. 2008; Bower et al. 2006; Khochfar et al. 2006), and HOD models (Hopkins et al. 2007), we record the fraction and rate of both major ($M1/M2 \geq 1/4$) and minor ($1/10 \leq M1/M2 < 1/4$) mergers between galaxies with stellar mass greater than $2.5 \times 10^{10} M_{\odot}$. These may be compared directly with our observed results. We also present results from the dissipationless N-body simulations of Donghia et al. (2008), which are for *dark matter halos* with mass 5×10^{12} – 10^{14} h^{-1} M$_{\odot}$. These are subject to the numerous uncertainties related to connecting galaxies with dark matter halos, discussed above. For the SPH simulations analyzed by Maller et al. (2006), we show the fraction and rate of major mergers (defined here as $1/3 \leq M1/M2 < 1/1$) among galaxies with stellar mass $3.0 \times 10^{10} < M_*/M_{\odot} < 2.2 \times 10^{11}$.

The limited dynamic range of the current simulations does not allow any predictions for minor mergers.

We find relatively good agreement within a factor of ∼ 2–3), for the total (major+minor) merger fraction f (Fig. 11), both between the data and models and between different models. This is rather remarkable given all the uncertainties involved in the model prescriptions for the treatment of substructure and baryonic physics. Separate comparisons with the major merger or minor merger fraction is more difficult as we only have lower limits from the observations.

However, we note that there is a wide range of over an order of magnitude in the predicted major merger rates R from different models, with the N-body models (Donghia et al 2008) and SPH models (Maller et al 2006) falling a factor of 10 below that of the SAMS and HOD modeling. This is not surprising, given that these simulations do not reproduce the observed number density of galaxies on the mass scales of interest (few $\times 10^{10} M_{\odot}$), and therefore absolute rates are not expected to match the observations. It is a well known problem that ΛCDM based models that do not include some kind of suppression of cooling in massive halos (e.g., due to AGN feedback) badly over-predict the number of massive galaxies.

4.6. The impact of galaxy interactions on the average SFR over the last 7 Gyr

The impact of galaxy interactions on the cosmic SF history of galaxies is of great astrophysical interest. The idea that galaxy interactions enhance the SFR of galaxies and trigger strong nuclear starbursts is well established from observations (e.g. Larson & Tinsley 1978; Joseph & Wright 1985; Kennicutt et al. 1987; Barton et al 2003) and simulations (e.g., Negroponte & White 1983; Hernquist 1989; Barnes & Hernquist 1991, 1996; Mihos & Hernquist 1994, 1996; Barnes 2004; Springel, Di Matteo & Hernquist 2005). However, simulations cannot robustly predict the impact of galaxy interactions on the SF activity of galaxies over the last 7 Gyr, since both the SFR and properties of the remnants in simulations are highly sensitive to the stellar feedback model, the bulge-to-disk (B/D) ratio, the gas mass fractions, and orbital geometry (e.g., Cox et al 2006; di Matteo et al. 2007).

We adopt the SFRs in Bell et al. (2005, 2007), based on Combo-17 UV data (Wolf et al. 2004) and deep Spitzer 24 μm observations with a limiting flux of ~ 83 μ Jy from the Spitzer Guaranteed Time Observers (Papovich et al. 2004; Gordon et al. 2005). The unobscured SFR based on the directly observable UV light from young stars was computed using $\mathrm{SFR_{UV}} = 9.8 \times 10^{-11}$ $(2.2\ L_{\mathrm{UV}})$, where $L_{\mathrm{UV}} = 1.5 \nu l_{\nu,2800}$ is a rough estimate of the total

integrated 1216–3000 Å UV luminosity, derived using the 2800 Å rest-frame luminosity from COMBO-17 $l_{\nu,2800}$. The factor of 1.5 used in converting the 2800 Å luminosity to total UV luminosity accounts for the UV spectral shape of a 100 Myr-old population with constant SFR. The factor of 2.2 corrects for the light emitted longward of 3000 Å and shortward of 1216 Å. The SFR calibration is derived from Pégase assuming a 100 Myr old stellar population with constant SFR and a Chabrier (2003) IMF.

The obscured SFR can be calculated from dust-reprocessed IR emission using the expression $\mathrm{SFR_{IR}} = 9.8{\times}10^{-11}\ L_{\mathrm{IR}}$, where L_{IR} is the total IR luminosity (TIR) over 8–1000 μm. L_{IR} is constructed from the observed 24 μm flux (corresponding to rest-frame wavelengths of 19–13 μm over $z \sim 0.24$–0.80) using the method outlined in Papovich & Bell (2002), based on an average Sbc template from the Devriendt et al. (1999) SED library. In converting from L_{IR} to $\mathrm{SFR_{TIR}}$, Bell et al. (2007) assume that the bulk of the 24 μm emission comes from SF, and not from AGN activity, based on the statistical result that less than 15% of the total 24 μm emission at $z < 1$ is in X-ray luminous AGN (e.g., Silva et al. 2004; Bell et al. 2005; Franceschini et al. 2005; Brand et al. 2006). Uncertainties in these SFR estimates are no less than a factor of 2 for individual galaxies while the systematic uncertainty in the overall SFR scale is likely to be less than a factor of 2 (Bell et al. 2007).

We investigate the star formation properties of the sample S2 of ∼3698 intermediate mass ($M \geq 1.0{\times}10^9\ M_\odot$) galaxies. This sample is complete for the blue cloud, but incomplete for the red sequence in the highest redshift bins (§ 2). However, since most of the SFR density originates from the blue cloud, this incompleteness does not have any major impact on the results. (Fig. 13 shows the UV-based SFR is plotted *versus* the stellar mass in each redshift bin. The UV-based SFR ranges from ~ 0.01 to 25 $M_\odot\ \mathrm{yr}^{-1}$, with most galaxies having a rate below 5 $M_\odot\ \mathrm{yr}^{-1}$.

While it is desirable to use the Spitzer 24 μm data in order to account for obscured star formation, only $\sim 24\%$ (~ 878 galaxies) of the 3698 galaxies in our intermediate mass sample have a Spitzer 24 μm detection, although over 86% of the sample is covered by the Spitzer observations down to a limiting flux of ~ 83 μ Jy. The detected galaxies yield a median ratio of $(\mathrm{SFR_{IR}}/\mathrm{SFR_{UV}})$ of ~ 3.6, indicative of a sustantial amount of obscured star formation.

The average UV-based SFR (based on 3698 galaxies) and UV+IR-based SFR (based on only the 878 galaxies with 24um detections) are plotted in the top 2 panels of Fig. 14 for three groups of intermediate mass galaxies: 'Interacting', 'Non-Interacting E-Sd' and 'Non-Interacting Irr1'. The value of $\mathrm{SFR_{UV+IR}}$ in the first redshfit bin looks anomalously high compared to the corresponding $\mathrm{SFR_{UV}}$. We suspect that this is due to excess 24 μm emission from an AGN component. It can be seen that over $z \sim 0.24$–0.80, the average UV-

based and UV+IR-based SFR of interacting galaxies *are only modestly enhanced*, at best by a factor of a few, compared to the non-interacting galaxies (Fig. 14; see also Robaina et al. in preparation). This modest enhancement is consistent with the recent statistical study of di Matteo et al. (2007), who find from numerical simulations of several hundred galaxy collisions that that the maximum SFR in galaxy mergers is typically only a factor of 2-3 larger than that of corresponding non-interacting galaxies. Their results suggest that the results of some early simulations (e.g., Mihos & Hernquist 1996; Hernquist & Mihos 1995), where mergers converted 50 to 80 per cent of their original gas mass into stars, may not represent the typical situation at $z < 1$.

In order to further test the robustness of our result, we used the stacking procedure described in Zheng et al. (2006) to get a more representative measure of the IR-based SFR for the following three groups of intermediate mass galaxies: 'Interacting', 'Non-Interacting E-Sd' and 'Non-Interacting Irr1'. For every group, the individual galaxies were cross-correlated with the Spitzer 24 μm catalog in order to identify detected and undetected objects. Then the PSF-removed 24 μm images for the undetected objects were stacked, and a mean flux was derived from the average/median stacked image. An average 24um luminosity was determined from the individually-detected fluxes and individually-undetected fluxes estimated by stacking. The 3217 intermediate mass galaxies in the Spitzer field were used in this process, giving a more representative 24um luminosity than the mere 878 galaxies with detections. A final uncertainty can be obtained by combining background error and bootstrap error in quadrature. The IR-based SFR was estimated from the 24um luminosity using the procedure described above, and combined with the UV-based SFR to estimate the total SFR. The average UV+IR-stacked SFR is plotted in the bottom panel of Fig. 14: the same: again only a modest enhancement of a factor of a few is seen in the average SFR of interacting galaxies, compared to non-interacting galaxies.

4.7. The contribution of interacting galaxies to the cosmic SFR density over the last 7 Gyr

Over the redshift interval $z \sim 0$ to 1, corresponding to the last 8 Gyr, the cosmic SFR density is claimed to decline by a factor of 3 to 10 (e.g., Madau et al. 1996, 1998; Cowie et al. 1996; Flores et al. 1999; Haarrsma et al. 2000). The reasons for this decline are not well understood. As a first step, we explore the relative contributions of interacting and non-interacting galaxies to the cosmic SFR density since $z < 1$.

Fig. 15 shows the SFR density for intermediate mass 'Interacting', 'Non-Interacting E-Sd' and 'Non-Interacting Irr1' galaxies over $z \sim 0.24$–0.80. The top panel shows the UV-

based SFR density from the full sample. The middle panel show the UV+IR-based SFR density from the 878 galaxies with individual 24um detections. Finally, the bottom panel shows the UV+IR-stacked SFR density determined via the stacking of 3817 galaxies with Spitzer coverage, as outlined in § 4.6. In all three panels, one finds that *interacting galaxies only account for a small fraction (< 30%) of the cosmic SFR density over $z \sim 0.24$–0.80, corresponding to lookback times of 3–7 Gyr (Fig. 14).* We again note that the anomalously high IR-based SFR of interacting galaxies in the first redshfit bin is likely due to excess 24 μm emission from an AGN component,

Thus, our results suggest that the behavior of the cosmic SFR density over $z \sim 0.24$–0.80 is predominantly shaped by non-interacting galaxies. This result is a direct consequence of the fact that the interaction interaction fraction f (Table 2; § 4.3), as well as the enhancement in the average SFR from interactions (§ 4.6), are both modest. Our results are consistent with the earlier findings that the UV (Wolf et al. 2005) and IR (Bell et al. 2005) luminosity density at $z \sim 0.65$–0.75 (lookback times of 6.2–6.8 Gyr) are dominated by non-interacting galaxies, but it is noteworthy that the interval studied here is a nearly a factor of seven larger, covering lookback times of 3 to 7 Gyr. Furthermore, our results agree remarkably well with models for the self-regulated growth of supermassive black holes in mergers involving gas-rich galaxies (Hopkins et al. 2005). These models predict that galaxy mergers contribute only $\sim 20\%$ of the SFR density of at $z \sim 1$, and even out out to $z \sim 2$.

It is legitimate to ask whether the results hold despite the uncertainties in identifying strongly interacting galaxies. We first note that based on the tests of § 4.1, we have already included a large fractional error term on f to account for the binomial standard deviation, the dispersion between classifiers, and the effect of moderate bandpass shifting, and surface brightness dimming. Therefore, the results presented here already take into account at least some of these sources of uncertainties.

Another source of uncertainty might be that some of the galaxies, which we have classified as 'Non-Interacting Irr1', under the assumption that their small-scale asymmetries that are likely caused by SF rather than interactions (§ 3.2), may be borderline cases of interacting galaxies. However, it can be seen from Fig. 15, that even if we were to add the SFR density of *all* the 'Non-Interacting Irr1' to that of the interacting galaxies, the sum would still be significantly lower than the contribution of 'Non-Interacting E to Sd' galaxies. Thus, the results would be largely unchanged.

Another test is to repeat the analyses using the CAS merger criterion ($A > 0.35$ and $A > S$) to identify interacting galaxies. The limited recovery rate (40% to 50%) and significant contamination impacting the CAS criterion (§ 3.4) make it more difficult to interpret the SF properties of systems identified as interacting or non-interacting with CAS. Fig. 16 shows

that the average SFR of 'CAS-interacting' galaxies is only modestly enhanced compared to 'CAS non-interacting' galaxies, in agreement with the results from § 4.6. Furthermore, Fig. 17 shows that 'CAS-interacting' galaxies contribute only 16% to 33% of the UV SFR density and 22% to 38% of the UV+IR SFR density. While the upper limits of these values are slightly higher than those based on the visual types, it is nonetheless reassuring that 'CAS non-interacting' galaxies' dominate the SFR density.

For intermediate mass ($M \geq 1.0 \times 10^9\ M_\odot$) galaxies, we find that the cosmic SFR density declines by a factor of ~ 3 from $z \sim 0.80$ to 0.24 (lookback time ~ 7 to 3 Gyr). Since non-interacting galaxies dominate the cosmic SFR density in every redshift bin, it follows that this decline *is largely the result of a shutdown in the SF of relatively non-interacting galaxies.* The question of what drives this shutdown will be addressed in detail in a future paper, and is only considered briefly here. One possibility is the depletion of the internal cold gas supply of galaxies by star formation, or the reduction in the accretion rate of gas from cosmological filaments. Future facilities like ALMA will be instrumental in exploring this issue further. Another related possibility is that over time, most of the SFR is shifting to lower stellar masses. This is illustrated in the dependence of the SFR (Fig. 13) and specific SFR (SSFR; Fig. 18) on stellar mass. High mass systems are associated with a lower SSFR (Fig. 18; see also Cowie et al. 1996; Brinchmann et al. 2004; Brinchmann & Ellis 2000; Fontana et al. 2003; Bauer et al. 2007), consistent with the idea that they have experienced the bulk of their stellar mass growth at earlier epochs ($z > 1$). In staged SF models (Noeske et al. 2007) the SF history of low mass systems is consistent with exponential SF models associated with an late onset and a long duration.

5. Summary and Conclusions

We explore the frequency and impact of interactions on the star formation of galaxies over $z \sim 0.24$–0.80 (lookback times of 3–7 Gyr), based on *HST* ACS, COMBO-17, and Spitzer 24 μm data from the GEMS survey. Our approach complements existing studies in several ways: (1) We use a large sample of ~ 3700 ($M \geq 1 \times 10^9\ M_\odot$) galaxies and ~ 790 high mass ($M \geq 2.5 \times 10^{10}\ M_\odot$) galaxies for robust number statistics (§ 2). (2) Two independent methods are used to identify strongly interacting galaxies: a tailored visual classification system complemented with spectrophotometric redshifts and stellar masses (§ 3.2), as well as the CAS merger criterion ($A > 0.35$ and $A > S$), based on CAS asymmetry A and clumpiness S parameters (§ 3.4). This allows the first systematic comparison to date between CAS-based and visual classification results (§ 4.2). (3) We set up the visual classification system (§ 3.2) so as to target strong interactions with mass ratio $M1/M2 > 1/10$. While

many earlier studies focused on major mergers, it is important to constrain minor mergers as well, since minor mergers dominate the merger rates in LCDM models at $z < 1$. Our results are:

1. Based on visual classification, the fraction f of interacting systems among high mass ($M \geq 2.5 \times 10^{10}\ M_{\odot}$) galaxies remains fairly constant over lookback times of 3–7 Gyr, ranging from 9% ± 5% at $z \sim 0.24$–0.34, to 8% ± 2% at $z \sim 0.60$–0.80, as averaged over every Gyr bin (Table 1; Fig. 11). The interacting galaxies are further subdivided into three categories: major ($M1/M2 > 1/4$), minor ($1/10 \leq M1/M2 < 1/4$) and major/minor interactions, with the last category containing ambiguous cases whose morphologies could be due to either a major or a minor interaction. We find a lower limit on the major merger/interaction fraction ranging from 1.1% ± 0.1% to 3.5% ± 2.2% over $z \sim 0.24$–0.80. The corresponding lower limit on the minor interaction fraction ranges from 3.6% ± 2.2% to 7.5% ± 2.7% (Table 1). Similar results are found for blue cloud intermediate mass ($M \geq 1.0 \times 10^{9}\ M_{\odot}$) galaxies (Table 2).

2. For our measured interaction fractions and assumed value of ~ 0.5 Gyr for the visibility timescale, it follows that *each massive ($M \geq 2.5 \times 10^{10}\ M_{\odot}$) galaxy has undergone ~ 0.7 interactions of mass ratio > 1/10 over the redshift interval $z \sim 0.24$–0.80. Of these 0.70 interactions we estimate that 0.19 are major mergers, 0.44 are minor mergers and the rest are either major or minor mergers.* The corresponding interaction rate R is a few $\times 10^{-4}$ galaxies Gyr^{-1} Mpc^{-3} (Fig. 12).

3. The interaction fraction based on the CAS merger criterion ($A > 0.35$ and $A > S$) agrees within a factor of two with the visually based interaction fraction for high mass ($M \geq 2.5 \times 10^{10}\ M_{\odot}$) galaxies. However, for intermediate mass ($M \geq 1 \times 10^{9}\ M_{\odot}$) galaxies, CAS can overestimate the interaction fraction at $z > 0.5$ by a factor ~ 3. In effect, the CAS criterion misses about half of the visually-classified strongly interacting galaxies, but picks up a significant number of non-interacting dusty, star-forming galaxies. This contamination will affect the integrated properties of interacting systems captured by CAS and these caveats must be borne in mind in studies that use CAS in blind automated mode.

4. We compare our results on the interaction history of high mass ($M \geq 2.5 \times 10^{10}\ M_{\odot}$) galaxies to predictions from different ΛCDM-based simulations of galaxy evolution, including halo occupation distribution (HOD) models, semi-analytic models (SAMs), and hydrodynamic simulations. To our knowledge, such extensive comparisons have not been attempted to date, and are long overdue. *We find relatively good agreement within a factor of $\sim$ 2–3, for the total (major+minor) merger fraction f (Fig. 11), both*

between the data and models and between different models. This is rather remarkable given all the uncertainties involved in the model prescriptions for the treatment of substructure and baryonic physics. However, *there are nearly two orders of magnitude variation in the predicted major merger rates from different models*, with some N-body and SPH models falling a factor of 10 below that of the SAMS and HOD modeling. This is likely related to the fact that these simulations do not reproduce the observed number density of galaxies on the mass scales of interest (few $\times 10^{10} M_{\odot}$), and therefore cannot match absolute observed merger rates. This issue is tied to to the known problem that ΛCDM based models, which do not include some kind of suppression of cooling in massive halos (e.g., due to AGN feedback) badly over-predict the number of massive galaxies.

5. We explore the impact of galaxy interactions on the SF properties of intermediate mass ($M \geq 1.0 \times 10^9\ M_{\odot}$) galaxies since $z < 0.8$. We find that *the average SFR of interacting galaxies is only modestly enhanced compared to non-interacting galaxies over $z \sim$ 0.24–0.80 (Fig. 14).* This result is found for SFRs based on UV, UV+IR, as well as UV+stacked-IR data. This modest enhancement is consistent with the recent statistical study of di Matteo et al. (2007) based on numerical simulations of several hundreds of galaxy collisions.

6. For intermediate mass ($M \geq 1.0 \times 10^9\ M_{\odot}$) galaxies, our results of a modest interaction fraction f and a modest enhancement in SFR from interactions culminate in our finding that strongly interacting systems only account for a small fraction ($< 30\%$) of the cosmic SFR density over $z \sim 0.24$–0.80 (lookback time $\sim$ 3–7 Gyr; Fig. 14). In effect, contrary to common lore, our results suggest that *the behavior of the cosmic SFR density over the last 7 Gyr is predominantly shaped by non-interacting galaxies, rather than strongly interacting galaxies.* We suggest that our observed decline in the cosmic SFR density by a factor of ~ 3 since $z \sim 0.80$ is largely the result of a shutdown in the SF of relatively non-interacting galaxies. This shutdown may be driven by the depletion of the internal cold gas supply of galaxies, the reduction in the accretion rate of gas from cosmological filaments, and the transition of SF activity to lower stellar masses.

S.J. acknowledges support from the National Aeronautics and Space Administration (NASA) LTSA grant NAG5-13063, NSF grant AST-0607748, and *HST* grants GO-10395 and GO-10861 from STScI, which is operated by AURA, Inc., for NASA, under NAS5-26555. Support for GEMS was provided by NASA through *HST* grant GO-9500 CH acknowledges the support of a European Commission Programme 6$^{\rm th}$ framework Marie Cure Outgoing

International Fellowship under contract M01F-CT-2006-21891. We thank Andrew Benson, Phil Hopkins, Sadegh Khochfar, Andi Burkert, and Ari Maller for useful discussions. This research has made use of NASA's Astrophysics Data System Service.

REFERENCES

Barazza, F. D., Jogee, S., & Marinova, I. 2007, IAU Symposium, 235, 76

Barden, M., et al. 2005, ApJ, 635, 959

Barden et al. 2008 ;tba

Barnes, J. E., & Hernquist, L. E. 1991, ApJL, 370, L65

Barnes, J. E., & Hernquist, L. 1996, ApJ, 471, 115

Barton Gillespie, E., Geller, M. J., & Kenyon, S. J. 2003, ApJ, 582, 668

Bell, E. F., et al. 2004, ApJL, 600, L11

Bell, E. F., et al. 2005, ApJ, 625, 23

Bell, E. F., Zheng, X. Z., Papovich, C., Borch, A., Wolf, C.,& Meisenheimer, K. 2007, ApJ, 663, 834

Benson, A. J., Lacey, C. G., Frenk, C. S., Baugh, C. M., & Cole, S. 2004, MNRAS, 351, 1215

Benson, A. J., Kamionkowski, M., & Hassani, S. H. 2005, MNRAS, 357, 847

Bershady, M. A., Jangren, A., & Conselice, C. J. 2000, AJ, 119, 2645

Binney, J., & Merrifield, M. 1998, Galactic astronomy / James Binney and Michael Merrifield. Princeton, NJ : Princeton University Press, 1998. (Princeton series in astrophysics) QB857 .B522 1998 ($35.00),

Binney, J., & Tremaine, S. 1987, Princeton, NJ, Princeton University Press, 1987, 747 p.,

Borch, A., et al. 2006, A&A, 453, 869

Bower, R. G., Benson, A. J., Malbon, R., Helly, J. C., Frenk, C. S., Baugh, C. M., Cole, S., & Lacey, C. G. 2006, MNRAS, 370, 645

Boylan-Kolchin, M., Ma, C.-P., & Quataert, E. 2008, MNRAS, 383, 93

Brand, K., et al. 2006,ApJ, 644, 143

Brand, K., et al. 2006,ApJ, 641, 140

Brinchmann, J., Charlot, S., White, S. D. M., Tremonti, C., Kauffmann, G., Heckman, T., & Brinkmann, J. 2004, MNRAS, 351, 1151

Brinchmann, J., & Ellis, R. S. 2000, ApJL, 536, L77

Chabrier, G. 2003, PASP, 115, 763

Cole, S., Lacey, C. G., Baugh, C. M., & Frenk, C. S. 2000, MNRAS, 319, 168

Conselice, C. J., Bershady, M. A., & Jangren, A. 2000, ApJ, 529, 886

Conselice, C. J., Bershady, M. A., Dickinson, M., & Papovich, C. 2003, AJ, 126, 1183

Conselice, C. J. 2006, ApJ, 638, 686

Cowie, L. L., Songaila, A., Hu, E. M., & Cohen, J. G. 1996, AJ, 112, 839

Cox, T. J., Jonsson, P., Primack, J. R., & Somerville, R. S. 2006, MNRAS, 373, 1013

Cox, T. J., Dutta, S. N., Di Matteo, T., Hernquist, L., Hopkins, P. F., Robertson, B., & Springel, V. 2006, ApJ, 650, 791

Cox, T. J., Di Matteo, T., Hernquist, L., Hopkins, P. F., Robertson, B., & Springel, V. 2006, ApJ, 643, 692

Croton, D. J., et al. 2006, MNRAS, 367, 864

Croton, D. J., et al. 2006, MNRAS, 365, 11

Devriendt, J. E. G., Guiderdoni, B., & Sadat, R. 1999, A&A, 350, 381

D'Onghia, E., & Burkert, A. 2004, ApJL, 612, L13

D'Onghia, E., Mapelli, M., Moore, B. 2008, MNRAS, submitted (arXiv:0803.0545)

di Matteo, P., Combes, F., Melchior, A.-L., & Semelin, B. 2007, A&A, 468, 6

Flores, H., et al. 1999, A&A, 343, 389

Flores, H., et al. 1999, ApJ, 517, 148

Fontana, A., et al. 2003, ApJL, 594, L9

Fontana, A., Poli, F., Menci, N., Nonino, M., Giallongo, E., Cristiani, S., & D'Odorico, S. 2003, ApJ, 587, 544

Franceschini, A., et al. 2005, AJ, 129, 2074

Gordon, K. D., et al. 2005, PASP, 117, 503

Governato, F., et al. 2004, ApJ, 607, 688

Hernquist, L. 1989, Nature, 340, 687

Hernquist, L., & Mihos, J. C. 1995, ApJ, 448, 41

Hopkins, P. F., Somerville, R. S., Hernquist, L., Cox, T. J., Robertson, B., & Li, Y. 2006, ApJ, 652, 864

Hopkins et al. 2008, ApJ, submitted (arXiv:0706.1243)

Jogee, S., Kenney, J. D. P., & Smith, B. J. 1999, ApJ, 526, 665

Jogee, S., 2006, Lecture Notes in Physics, Vol. 693, "AGN Physics on All Scales", Eds. D. Alloin, R. Johnson, & P. Lira (Springer: Berlin Heidelberg New York), Vol 93, Chapter 6, p 143 (astro-ph/0408383).

Joseph, R. D., & Wright, G. S. 1985, MNRAS, 214, 87

Kartaltepe, J. S., et al. 2007, ApJS, 172, 320

Kauffmann, G., White, S. D. M., & Guiderdoni, B. 1993, MNRAS, 264, 201

Kautsch, S. J., Grebel, E. K., Barazza, F. D., & Gallagher, J. S., III 2006, A&A, 451, 1171

Kennicutt, R. C., Roettiger, K. A., Keel, W. C., Vanderhulst, J. M., & Hummel, E. 1987, NASA Conference Publication, 2466, 401

Kennicutt, R. C., Jr., Roettiger, K. A., Keel, W. C., van der Hulst, J. M., & Hummel, E. 1987, AJ, 93, 1011

Khochfar, S., & Burkert, A. 2001, ApJ, 561, 517

Khochfar, S., & Burkert, A. 2005, MNRAS, 359, 1379

Khochfar, S., & Silk, J. 2006, MNRAS, 370, 902

Koopmann, R. A., & Kenney, J. D. P. 1998, ApJL, 497, L75

Larson, R. B., & Tinsley, B. M. 1978, ApJ, 219, 46

Le Fèvre, O., et al. 2000, MNRAS, 311, 565

Lin, L., et al. 2004, ApJL, 617, L9

Lotz, J. M., et al. 2008, ApJ, 672, 177

Madau, P., Ferguson, H. C., Dickinson, M. E., Giavalisco, M., Steidel, C. C., & Fruchter, A. 1996, MNRAS, 283, 1388

Madau, P., della Valle, M., & Panagia, N. 1998, MNRAS, 297, L17

Maller, A. H., Katz, N., Kereš, D., Davé, R., & Weinberg, D. H. 2006, ApJ, 647, 763

Mihos, J. C., Walker, I. R., Hernquist, L., Mendes de Oliveira, C., & Bolte, M. 1995, ApJL, 447, L87

Mihos, J. C., & Hernquist, L. 1994, ApJ, 437, 611

Mihos, J. C., & Hernquist, L. 1996, ApJ, 464, 641

Miller, S. H., et al. 2008, ArXiv e-prints, 802, arXiv:0802.3917

Murali, C., Katz, N., Hernquist, L., Weinberg, D. H., & Davé, R. 2002, ApJ, 571, 1

Naab, T., & Burkert, A. 2001, ApJL, 555, L91

Navarro, J. F., & Benz, W. 1991, ApJ, 380, 320

Navarro, J. F., & Steinmetz, M. 2000, ApJ, 538, 477

Navarro, J. F., & Steinmetz, M. 2000, ApJ, 528, 607

Negroponte, J., & White, S. D. M. 1983, MNRAS, 205, 1009

Noeske, K. G., et al. 2007, ApJL, 660, L47

Patton, D. R., Carlberg, R. G., Marzke, R. O., Pritchet, C. J., da Costa, L. N., & Pellegrini, P. S. 2000, ApJ, 536, 153

Patton, D. R., et al. 2002, ApJ, 565, 208

Rieke, G. H., et al. 2004, ApJS, 154, 25

Rix, H.-W., et al. 2004, ApJS, 152, 163

Robertson, B., Yoshida, N., Springel, V., & Hernquist, L. 2004, ApJ, 606, 32

Somerville, R. S., & Primack, J. R. 1999, MNRAS, 310, 1087

Somerville, R. S. & Kolatt, T. S. 1999, MNRAS, 305, 1

Somerville, R. S., et al. 2008, ApJ, 672, 776

Springel, V., Di Matteo, T., & Hernquist, L. 2005, MNRAS, 361, 776

Springel, V., Di Matteo, T., & Hernquist, L. 2005, MNRAS, 361, 776 '

Struck, C. 1997, ApJS, 113,269

Weinzirl, T., Jogee, S., Khochfar, S., Burkert, A., & Kormendy, J. 2008, ApJ, submitted.

Wolf, C., et al. 2004, A&A, 421, 913

Wolf, C., et al. 2005, ApJ, 630, 771

Zheng et al. 2006, ApJ, 640, 784

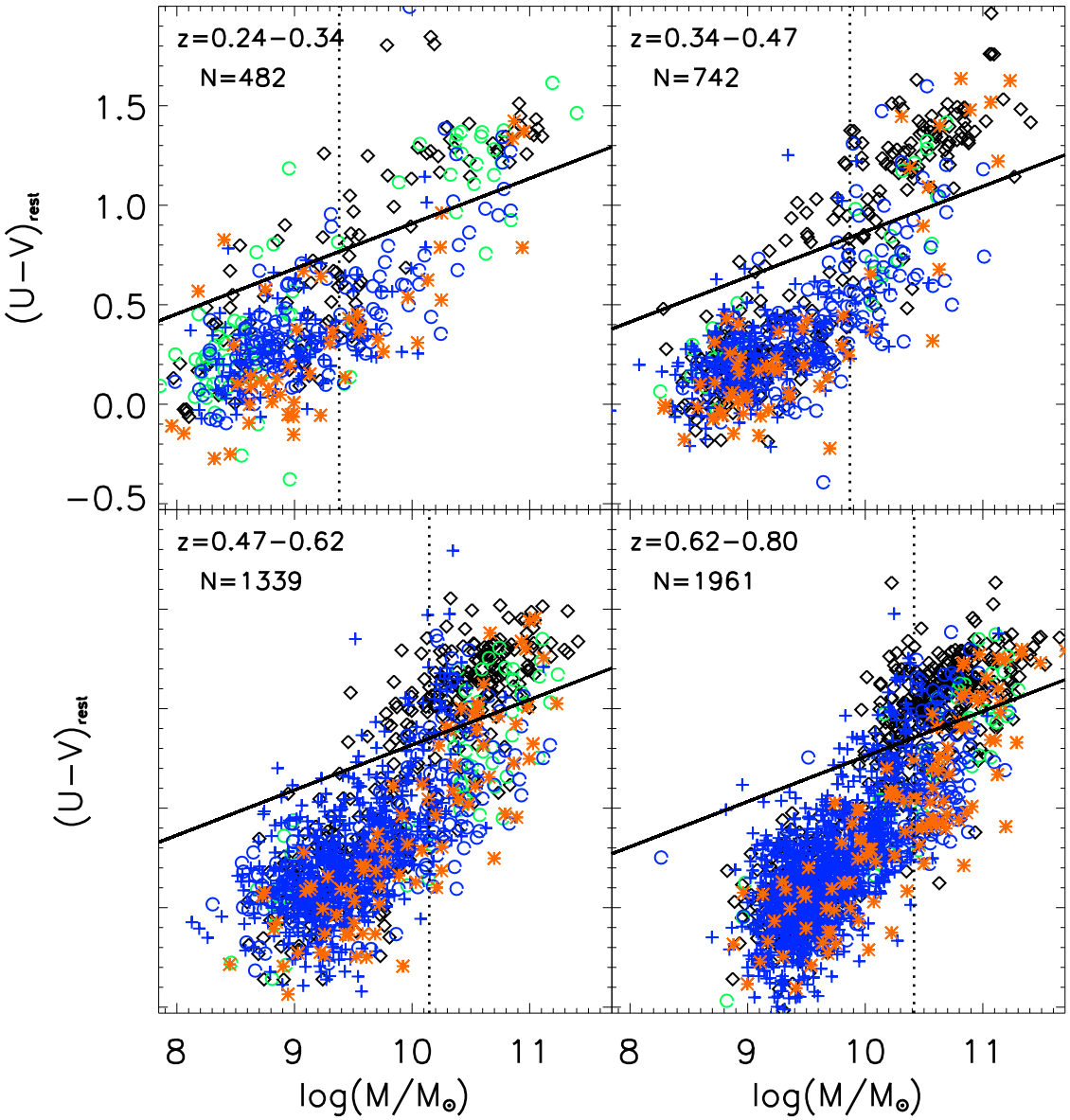

Fig. 1.— The rest-frame $U-V$ color is plotted *versus* the stellar mass in four redshift bins, which span 1 Gyr each, and cumulatively cover the interval $z \sim 0.24$–0.80 ($T_{\rm back} \sim 3$–7 Gyr). N denotes the number of galaxies in each bin. The diagonal line marks the separation of the red sequence galaxies and the blue cloud galaxies at the average redshift $z_{\rm ave}$ of the bin. The vertical lines marks the mass completeness limit (Borch et al. (2006) for the red sequence galaxies. The blue cloud galaxies are complete well below this mass. Galaxies are coded according to their visual type (VT) in the F606W band: 'Interacting' (orange stars), 'Non-Interacting E-Sd' (E+S0=black diamonds, Sa=green circles, Sb-Sc=blue circles, Sd=blue crosses), and 'Non-Interacting Irr1' (blue crosses) galaxies.

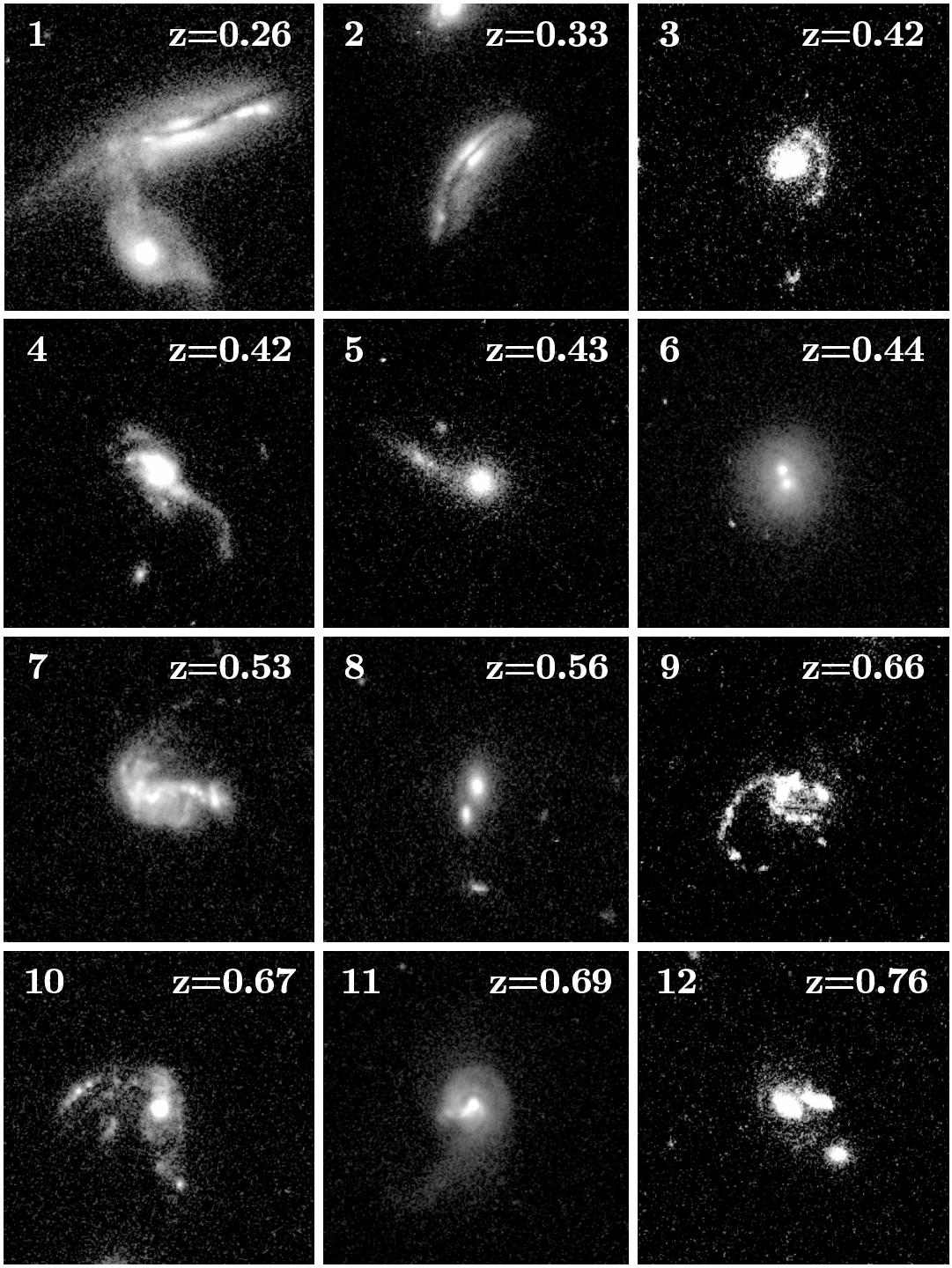

Fig. 2.— This montage show examples of galaxies classified as interacting ('Int') galaxies. These are candidates for a recent/ongoing interaction of mass ratio $M1/M2 > 1/10$. Systems classified as 'Int-1' show morphological distortions, such as multiple nuclei (e.g., 6, 8) or components (e.g., 12) connected by a bridge or common envelope, warped disks (e.g., 2), tidal tails (e.g., 3, 4, 5, 9, 11), strongly asymmetric features, or accreting companions (e.g., 1, 12). The lower galaxy in case 1 is an example of an 'Int-2' system or contact pair: it is *fairly symmetric*, but it has a companion, which satisfies four criteria: it has the same Combo-17 spectrophotometric redshift within the accuracy $\delta_z/(1+z) \sim 0.02$, has a stellar

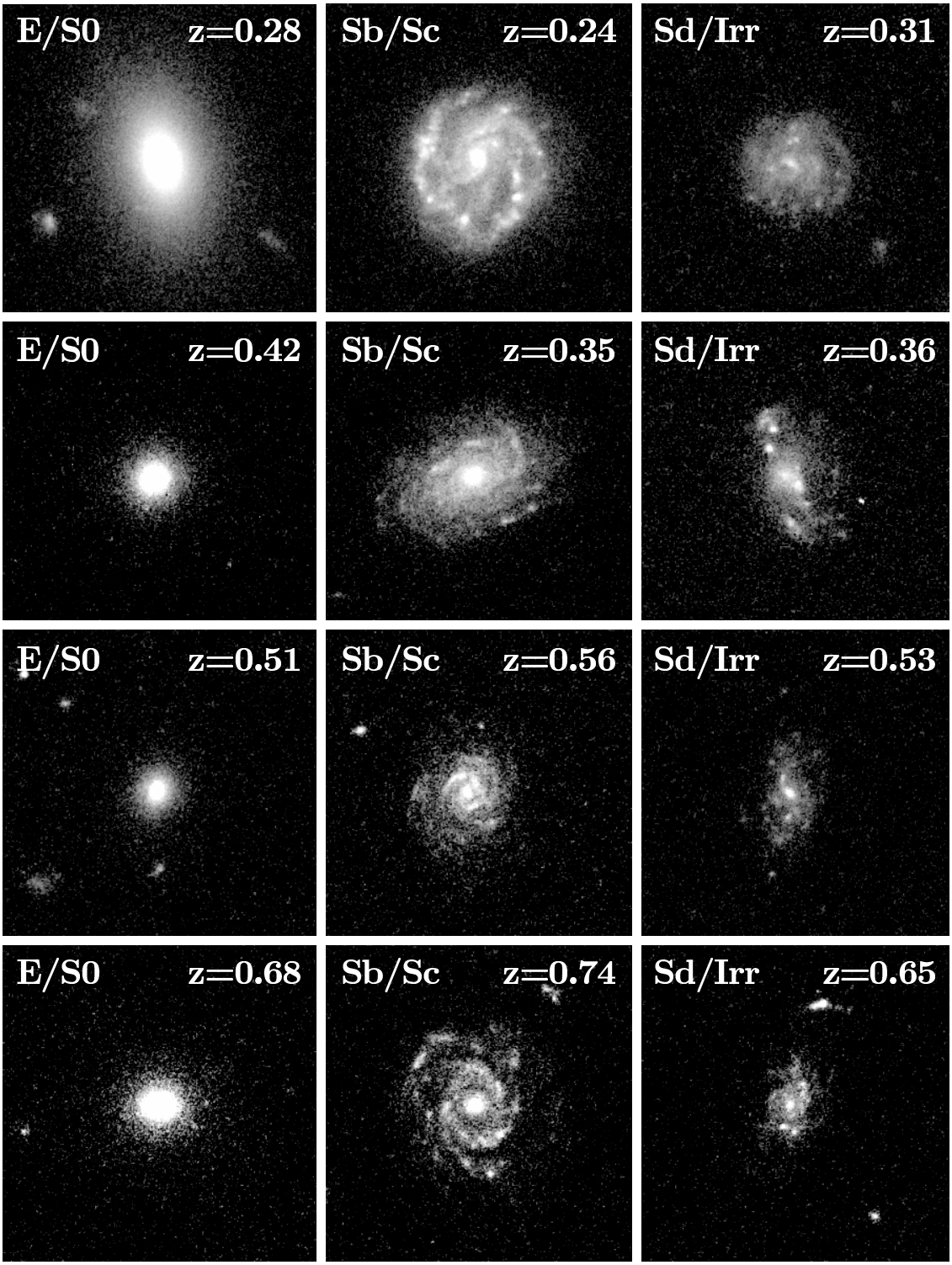

Fig. 3.— This montage shows examples of galaxies classified as 'Non-Interacting E-Sd' and ' Non-Interacting Irr1' galaxies. They are subdivided as E/S0, Sb/Sc and Sd/Irr1. The four rows show candidates from the four redshift bins in Figure 1.

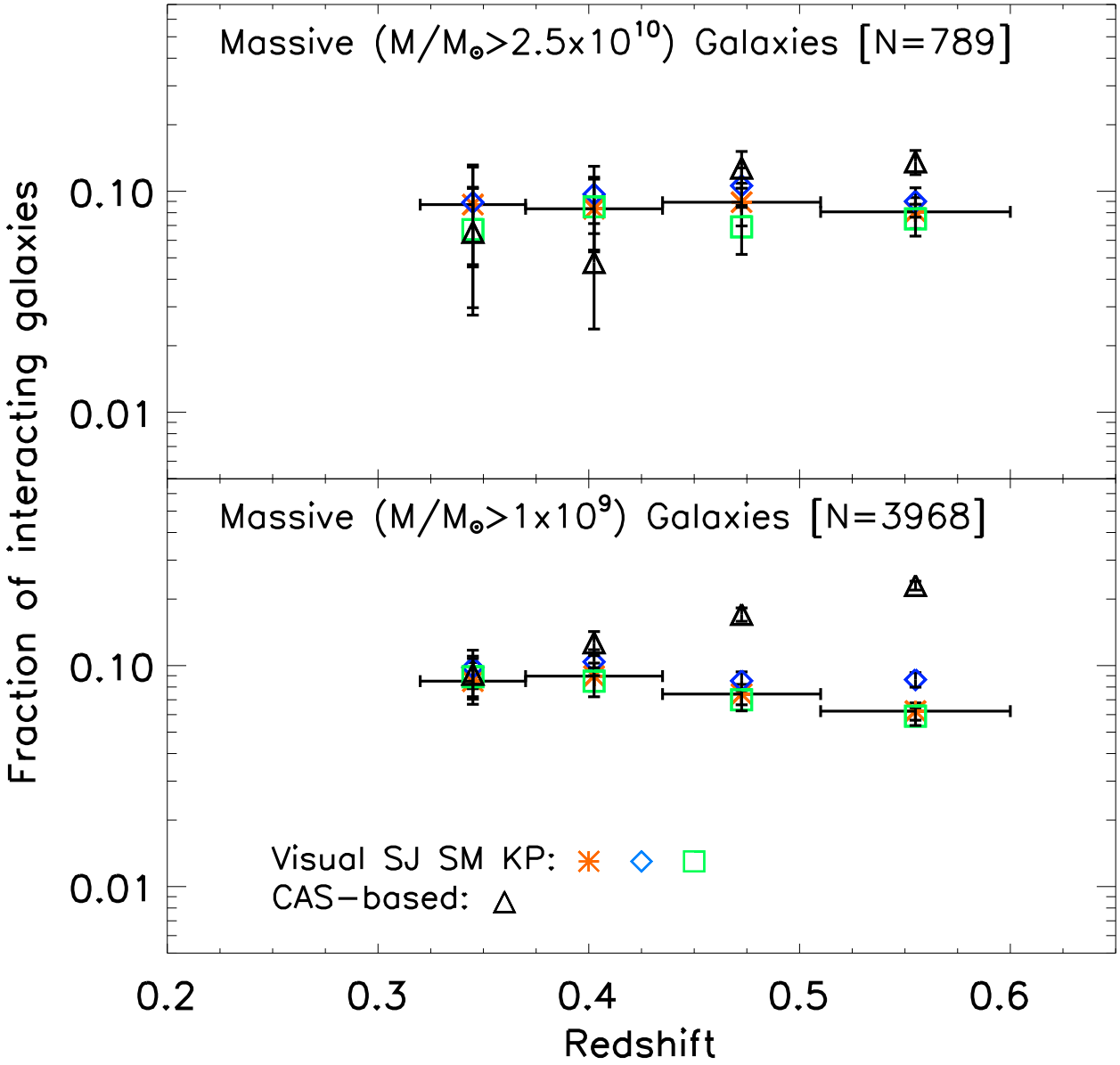

Fig. 4.— This figure compares the fraction (f) of strongly interacting galaxies,, based on visual classification by 3 classifiers (SJ, SM, KP), to the interaction fraction ($f_{\rm CAS}$) that would be obtained using the CAS criterion ($A > 0.35$ and $A > S$). The results are shown for both high mass ($M \geq 2.5 \times 10^{10}$ $M_\odot$; top panel) and intermediate mass ($M \geq 1 \times 10^9$ $M_\odot$; bottom panel) sample. The plotted error bar for f, at this stage, only includes the binomial term $[f(1\text{-}f)/N)]^{1/2}$, for each bin of size N. The same trend is seen for all 3 classifiers and the maximum spread $\delta_{\rm f}/f$ in the 4 bins is $\sim 26\%$. $f_{\rm CAS}$ agrees within a factor of two with the visually based f interaction fraction for high mass galaxies. However, for intermediate mass galaxies, CAS can overestimate the interaction fraction at $z > 0.5$ by a factor ~ 3, as it picks up a significant number of non-interacting dusty, star-forming galaxies (see § 4.2).

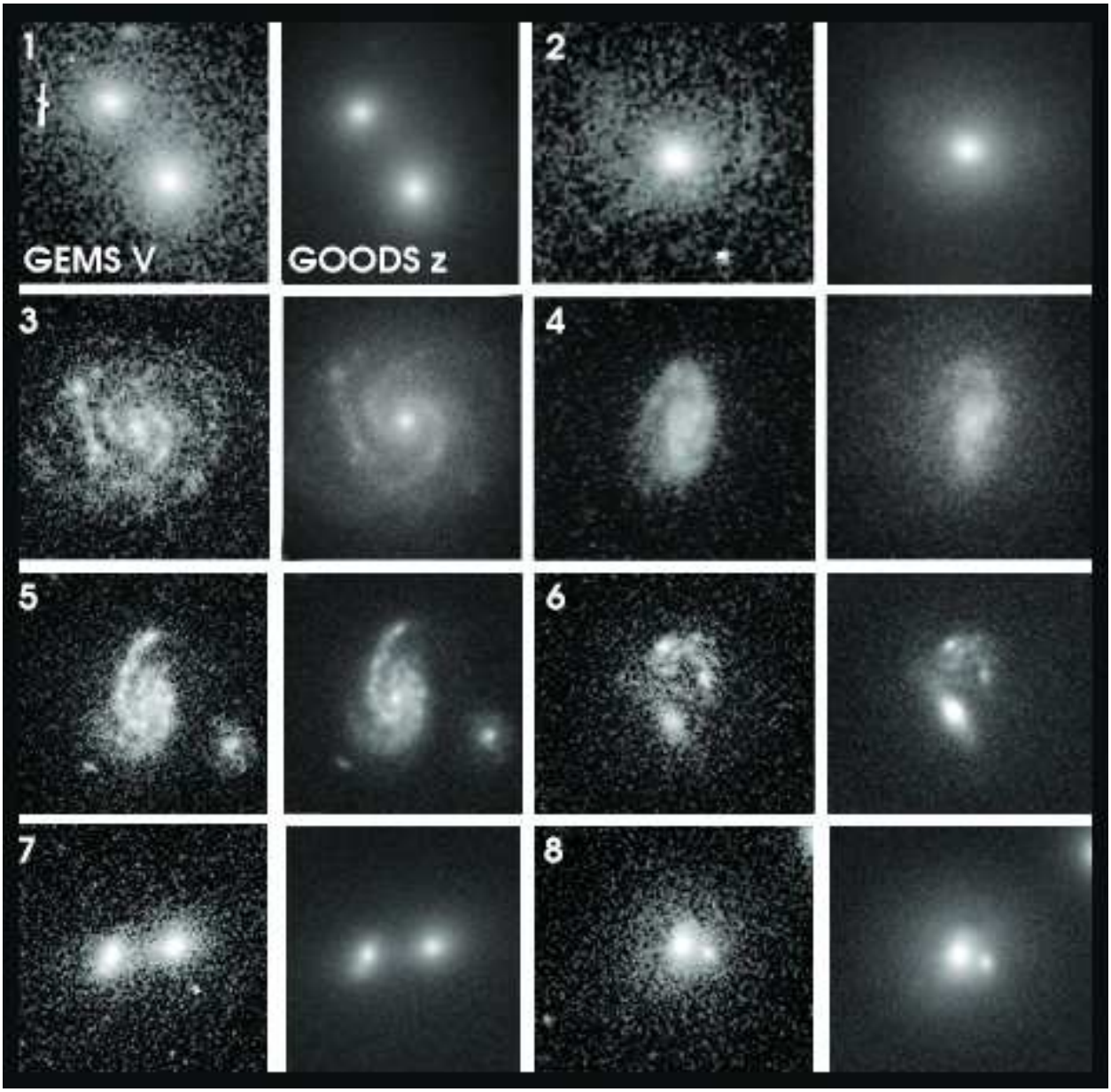

Fig. 5.— This montage illustrates a test for bandpass shift and surface brightness dimming. It compares the bluer shallower GEMS F606W images (V band; pivot $\lambda \sim 5915$ Å) and deeper redder GOODS F850LP (z band; pivot $\lambda \sim 9103$ Å) images of typical interacting and non-interacting galaxies in the last redshift bin ($z \sim 0.60$ to 0.80), where bandpass shift and surface brightness dimming are expected to be most severe. In this redshift bin, the rest-frame wavelength traced by the GEMS images shift from optical to violet/near-UV (3700 Å to 3290 Å). However, while the GOODS images have higher S/N, and trace redder older stars, they do not reveal dramatically different morphologies from from those in the GEMS F606W images. A statistical analysis is shown in Table 3.

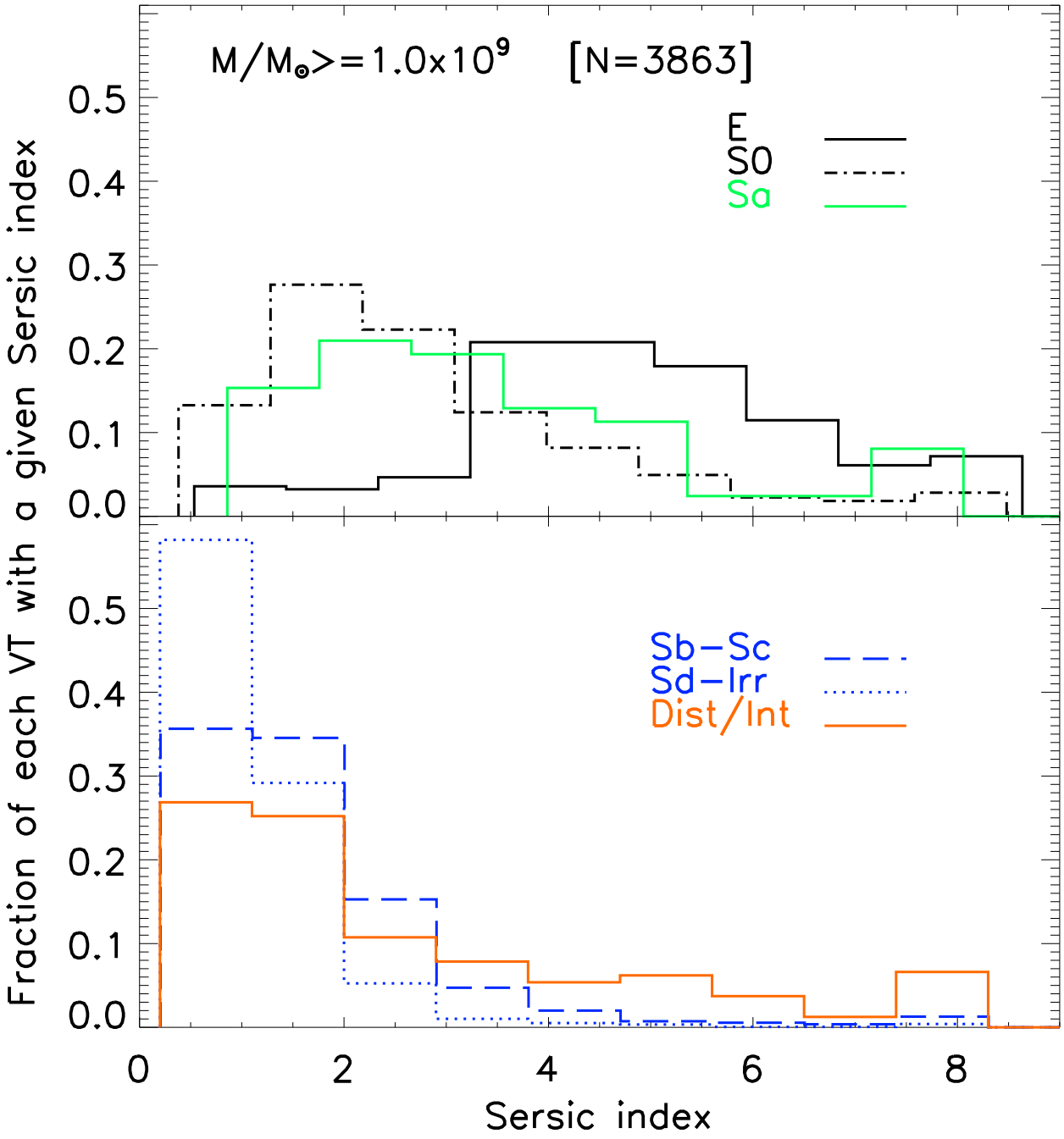

Fig. 6.— For intermediate mass ($M \geq 1 \times 10^9\ M_\odot$) galaxies, the distribution of Sérsic indices n from single-component Sérsic fits is plotted for interacting , 'non-Interacting E-Sd' and 'non-Interacting Irr1' galaxies. The latter classes are further subdivided as E/S0, Sb/Sc and Sd/Irr1. The majority of systems visually classified as Sb-Sc and Sd-Irr have $n < 2.5$, as expected for disk-dominated systems. Most of the systems visually typed as E have $n > 3$ and their distribution peaks at $n \sim 4$, corresponding to a de Vaucouleurs profile. S0 and Sa systems have intermediate n values. [THIS FIGURES NEEDS TO BE REPLACED WITH THE NEW ONE].

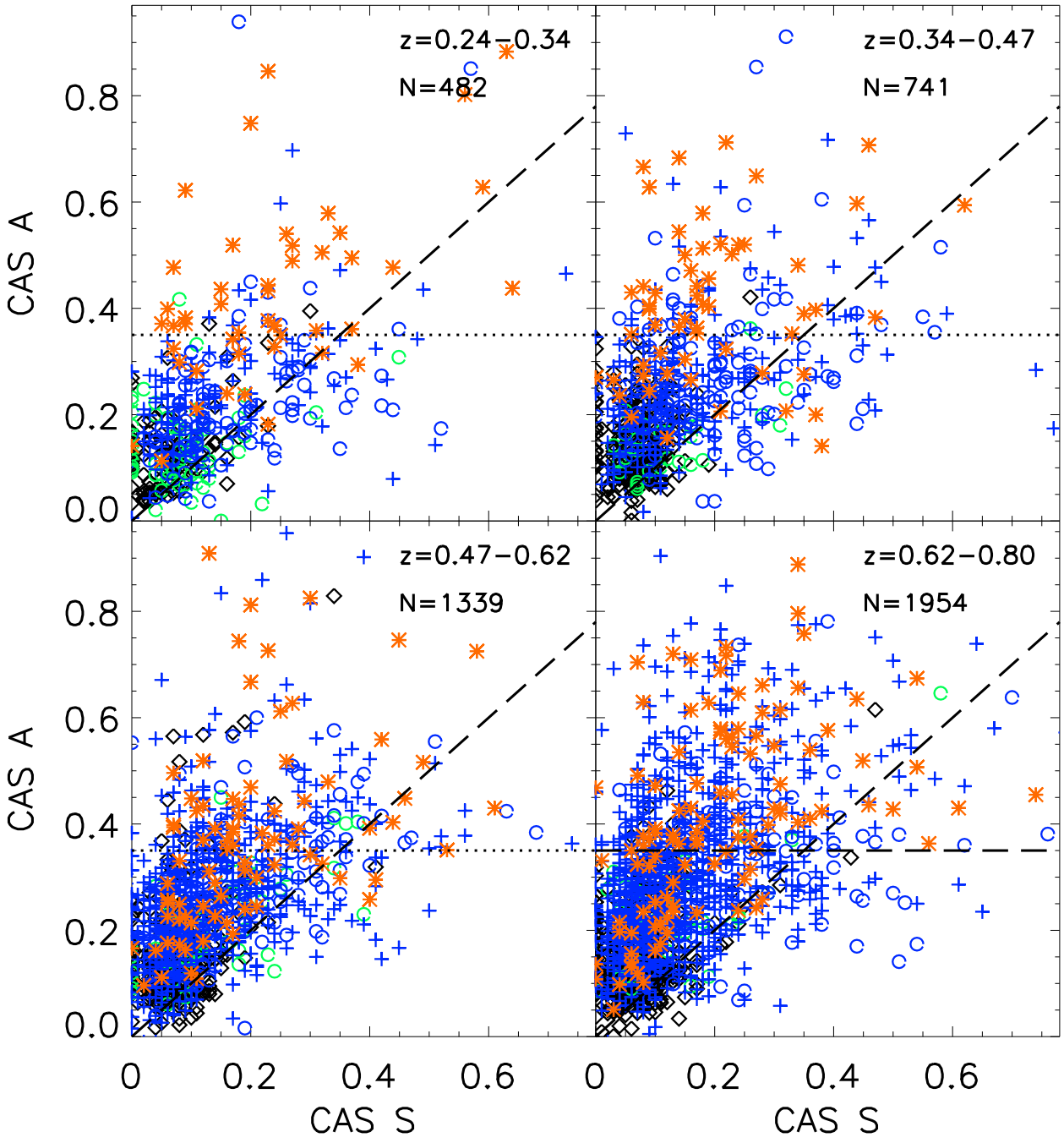

Fig. 7.— The CAS asymmetry A and clumpiness S parameters are plotted for galaxies in the four redshift bins of Fig. 1, using the same color coding. Galaxies satisfying the CAS criterion ($A > 0.35$ and $A > S$) lie in the upper left hand corner, bracketed by the $A = S$ diagonal line and the $A = 0.35$ horizontal line. The CAS criterion captures a fair fraction (40% to 50%) of the strongly interacting galaxies, but it also picks up "contaminants" in the form of non-interacting galaxies. This is further illustrated in Fig. 8.

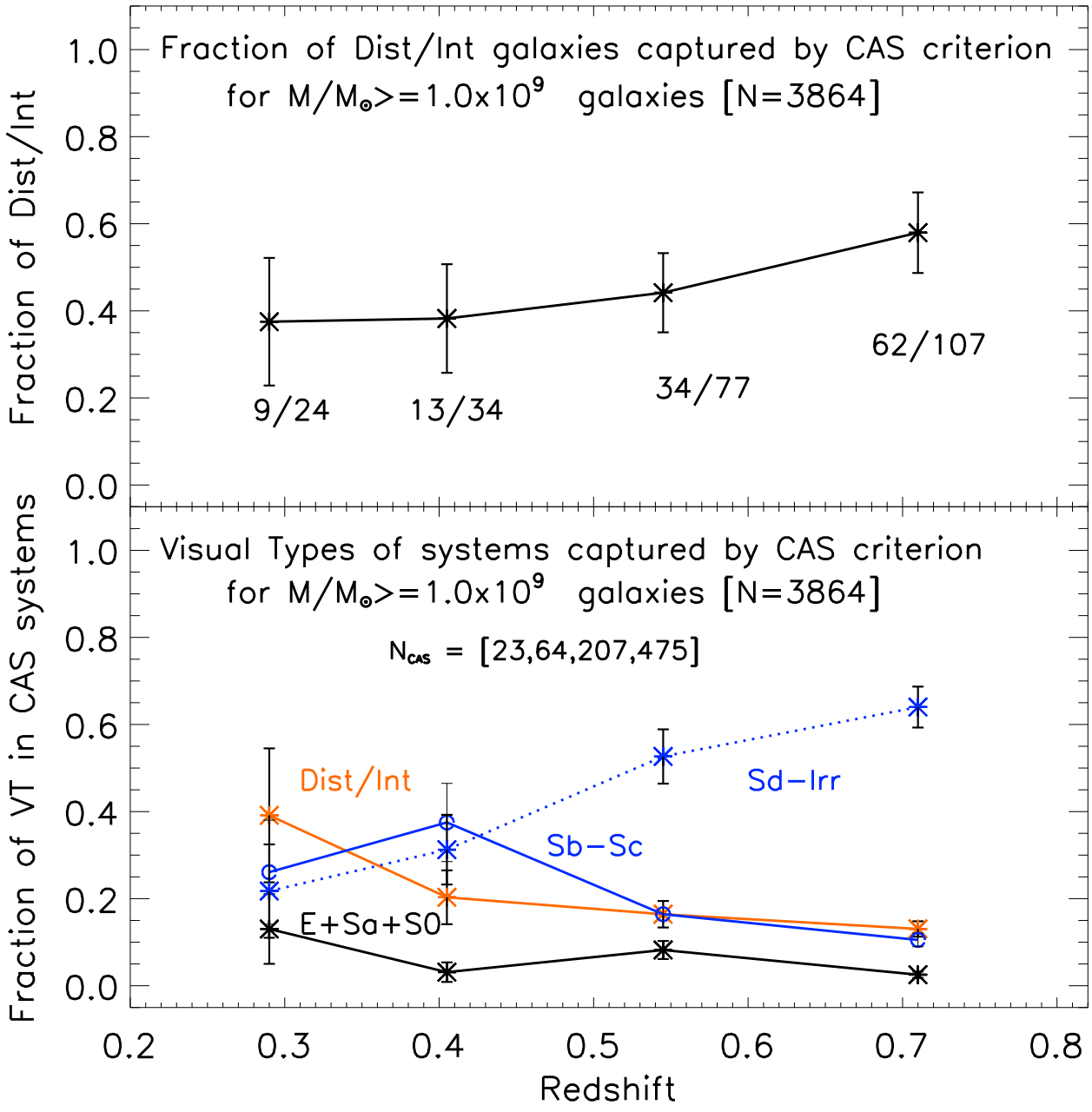

Fig. 8.— The top panel shows the fraction of strongly disturbed (Dist) systems captured by the CAS criterion ($A > 0.35$ and $A > S$) for the intermediate mass ($M/M_{\odot} \geq 1.0 \times 10^9$) sample. About 40% to 50% of the Dist systems are captured across the four redshift bins. The bottom panel shows the contamination level of the CAS system. $N_{\rm CAS}$ represents the number of systems picked up by the CAS criterion in the four redshift bins. The distribution of visual types among these systems is plotted. The vast majority (65% to 85%) of sytems picked up by CAS at $z > 0.5$ are non-interacting systems [Sd-Irr, Sb-Sc].

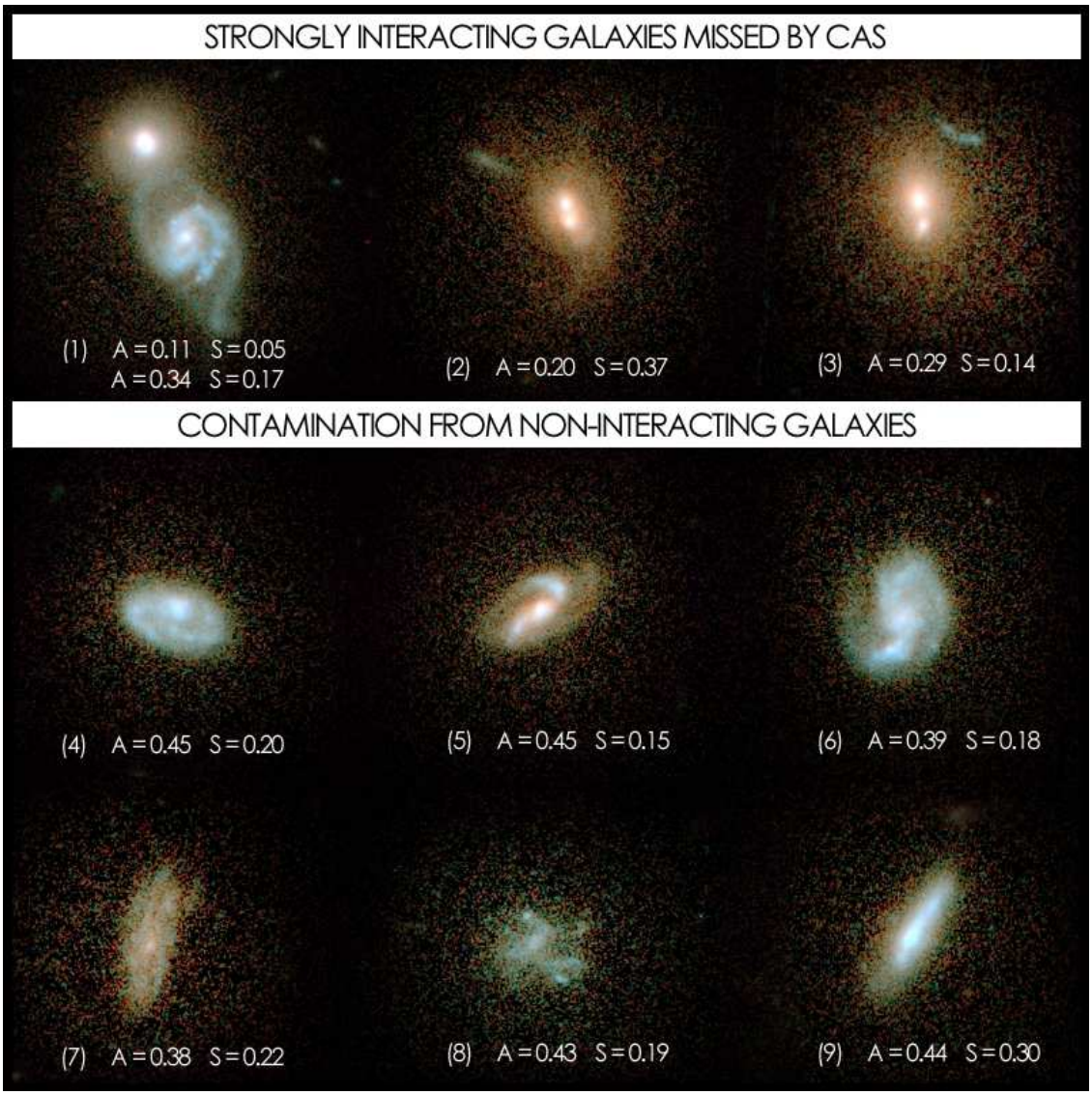

Fig. 9.— The montage shows typical systems where the CAS criterion ($A > 0.35$ and $A > S$) fails. Cases 1-3 are systems, which are visually classified as strongly interacting, but are missed by the CAS criterion. They include galaxies with tidal debris (Case 3), close double nuclei (case 2), and galaxies at the same redshift connected via tidal features (case 1). Conversely, cases 4-9 are systems, which are visually classified as non-interacting galaxies, but are picked by the CAS criterion. They include non-interacting, actively star-forming systems with small-scale asymmetries in the optical blue light (cases 4 and 6); systems where A is high due to the absence of a clear center (case 8) or due to the center being blocked by dust (case 4, 9); edge-on systems and compact systems, where the light profile is steep such that small centering inaccuracies lead to large A (case 9).

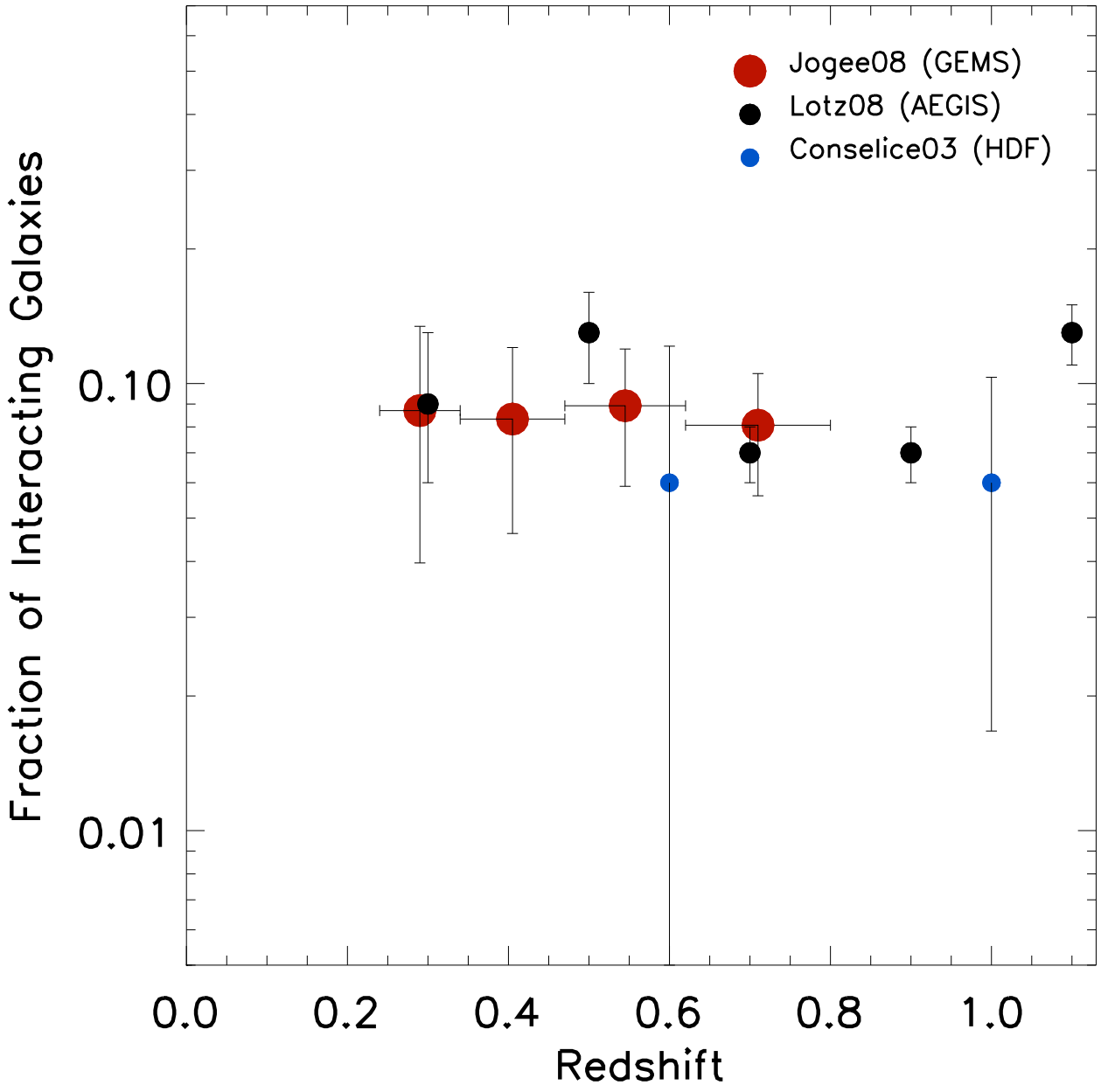

Fig. 10.— The observed fraction f of interacting galaxies in the high mass ($M \geq 2.5 \times 10^{10}$ $M_{\odot}$) sample is compared to other studies, noting the caveats outlined in § 4.4. Shown here is the fraction of morphologically disturbed systems based on Gini-M20 parameters among $M_{\rm B} <$ -20.5 and $L_{\rm B} > 0.4$ L_{*} galaxies in the Extended Groth Strip (Lotz et al. (2008). The CAS-based results from Conselice (2003) are derived from a small sample in the Hubble Deep Field.

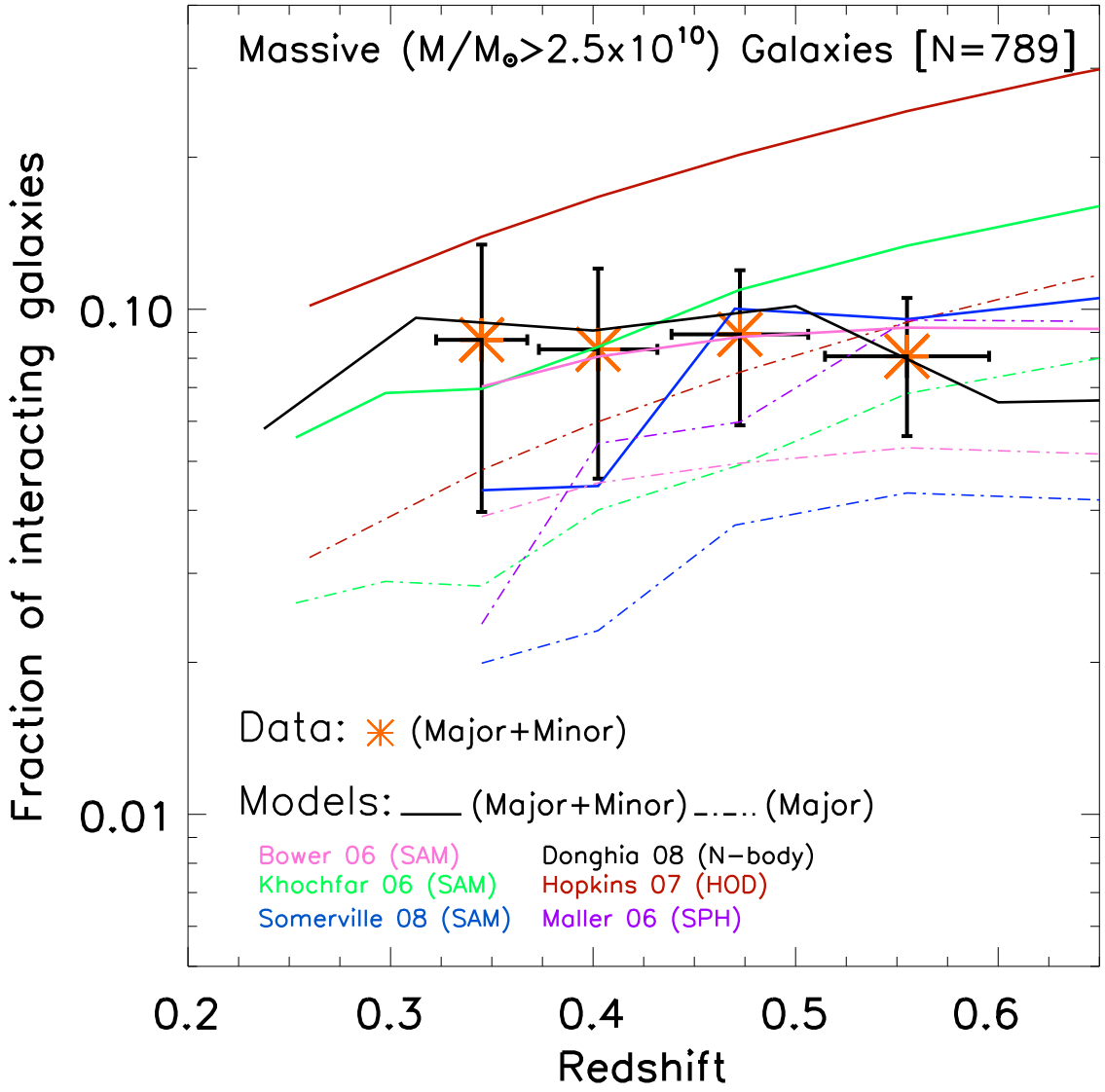

Fig. 11.— The observed fraction f of high mass interacting galaxies (orange stars) represents an estimate of the fraction of recent interactions of mass ratio $M1/M2 > 1/10$. It is compared to the fraction of (major+minor) mergers (solid lines; stellar mass ratio $M1/M2 > 1/10$) predicted by different ΛCDM-based simulations of galaxy evolution, including halo occupation distribution (HOD) models, semi-analytic models (SAMs), and hydrodynamic simulations. Models shown include three independent SAMs from Somerville et al. (2008), Bower et al. (2006), and Khochfar & Silk (2006); HOD models from Hopkins et al. (2007); smoothed particle hydrodynamics (SPH) cosmological simulations from Maller et al. (2006); and dissipationless N-body simulations of Donghia et al. (2008), which are for *dark matter halos* with mass 5×10^{12} – 10^{14} $h^{-1}M_{\odot}$. Remarkably, we find relatively good agreement within a factor of $\sim$ 2–3, for the total (major+minor) merger fraction f, both between the data and models, and between different models.

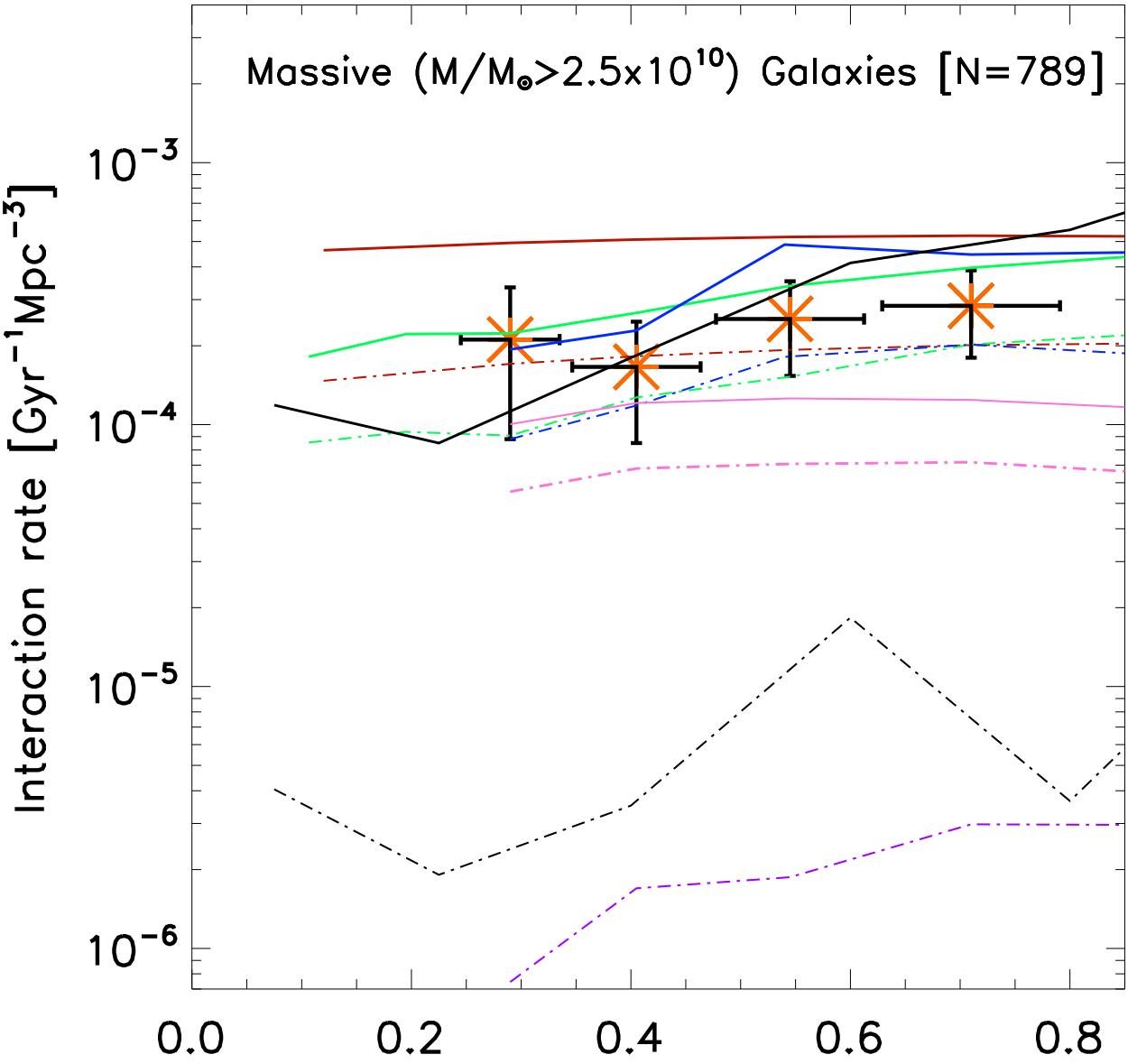

Fig. 12.— As in Fig. 11, but for the interaction rate R of high mass galaxies. Note that there is a striking two orders of magnitude variation in the predicted major merger rates from different models, with some N-body and SPH models falling a factor of 10 below that of the SAMS and HOD modeling. See § 4.5 for a discussion of the reasons behind the discrepancy.

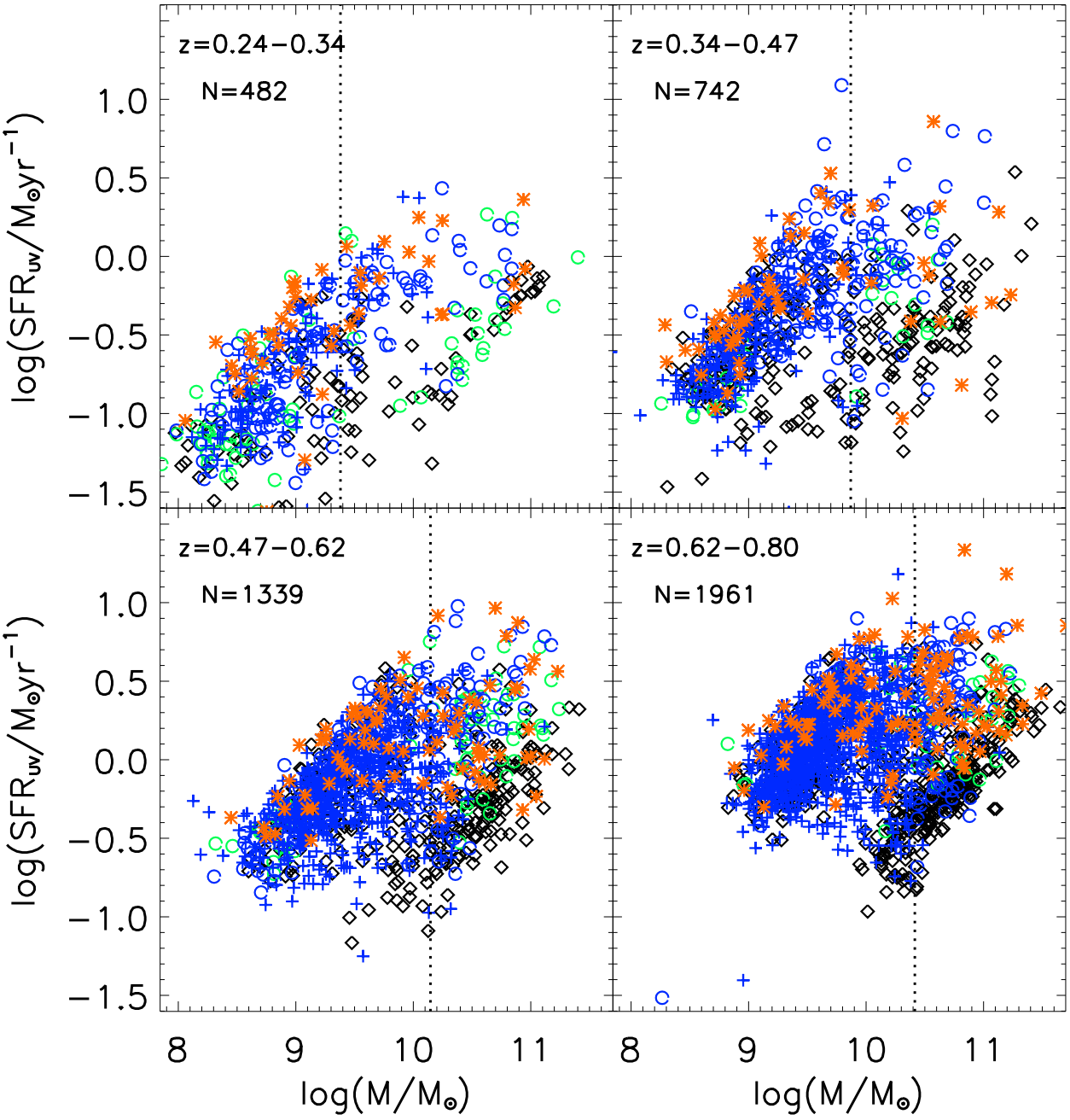

Fig. 13.— The UV-based star formation rate is plotted *versus* the stellar mass in four redshift bins, which span 1 Gyr each, and cumulatively cover the interval $z \sim 0.24$–0.80 ($T_{\rm back} \sim 3$–7 Gyr). N denotes the number of galaxies plotted in each bin. Galaxies are coded as in Fig. 1, with strongly interacting systems denoted by orange stars. The average SFR and total SFR density in both the UV and the IR, are further illustrated in Fig. 14 and Fig. 15.

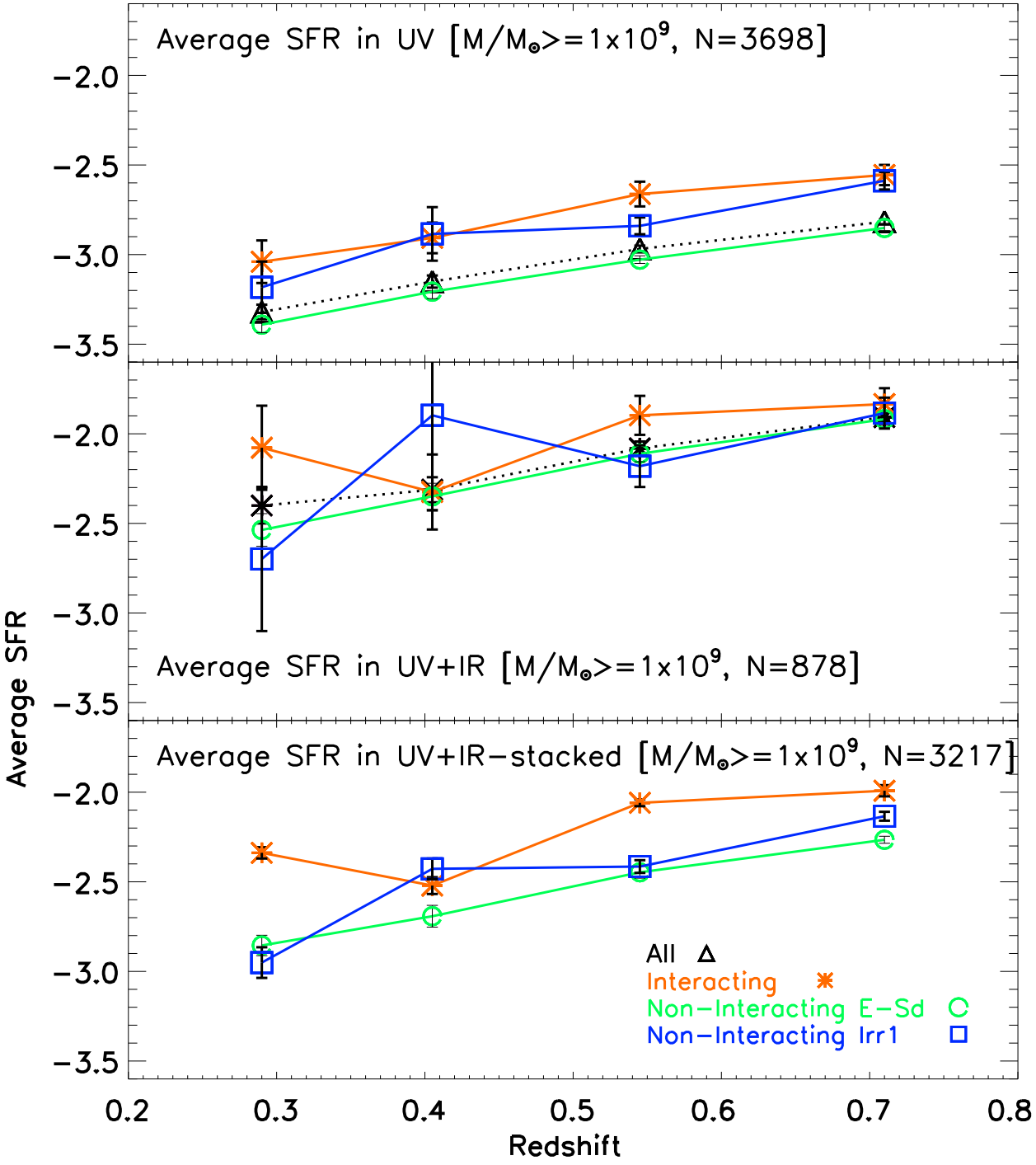

Fig. 14.— The average SFR of interacting, 'non-interacting E-Sd', and 'non-interacting Irr1' galaxies are compared over $z \sim 0.24$–0.80 for intermediate mass ($M \geq 1.0 \times 10^9\ M_\odot$) galaxies. N denotes the number of galaxies used. The average UV-based SFR (top panel; based on 3698 galaxies), average UV+IR-based SFR (middle panel; based on only the 878 galaxies with 24um detections), and average UV+IR-stacked SFR (based on 3213 galaxies with 24um coverage) are shown. In all there cases, the average SFR of interacting galaxies is only modestly enhanced compared to non-interacting galaxies over $z \sim 0.24$–0.80 (lookback time $\sim$ 3–7 Gyr).

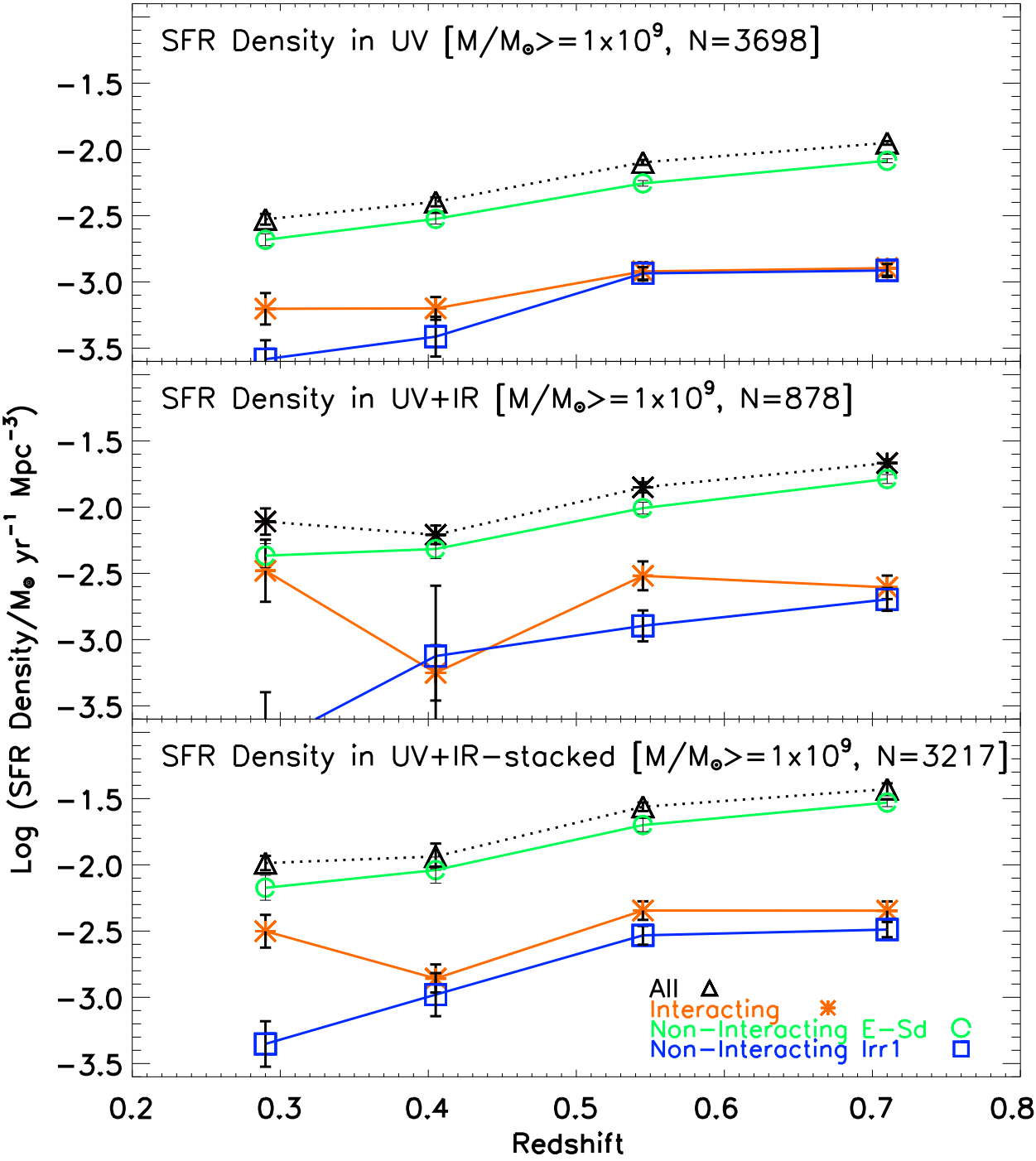

Fig. 15.— The SFR density of interacting, 'non-interacting E-Sd', and 'non-interacting Irr1' galaxies are compared over $z \sim 0.24$–0.80 for intermediate mass ($M \geq 1.0 \times 10^9\ M_\odot$) galaxies. Results based on UV (top panel), UV+IR (middle panel), as well as UV+stacked-IR data (bottom panel), are shown in the top, middle, and bottom panels. In all bins, strongly interacting galaxies only contribute a small fraction (typically below 30%) of the total SFR density. In effect, the behavior of the cosmic SFR density over the last 7 Gyr is predominantly shaped by non-interacting E-Sd galaxies rather than strongly interacting galaxies.

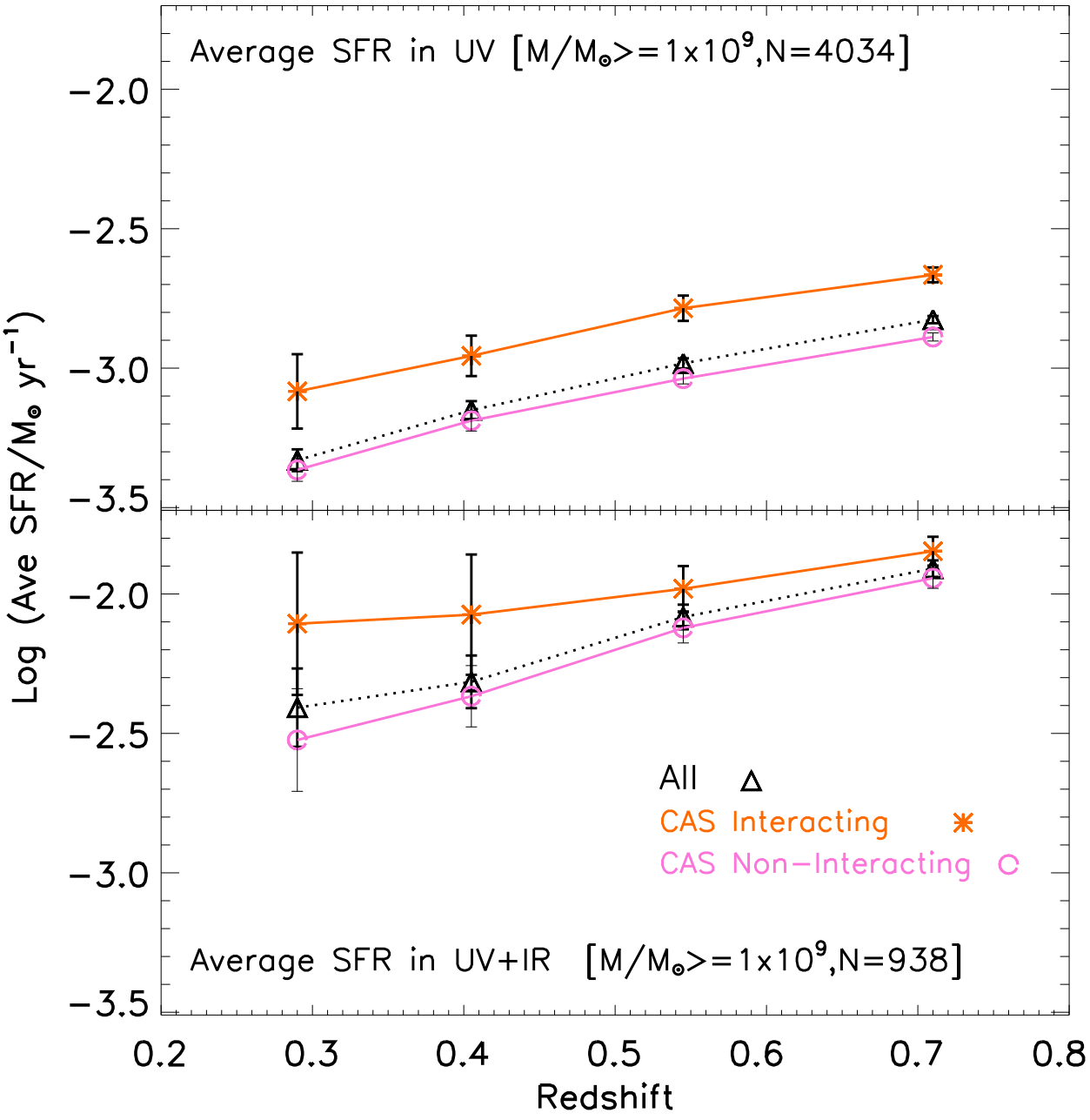

Fig. 16.— Same as in Fig. 14, but using the CAS merger criterion ($A > 0.35$ and $A > S$) to identify interacting galaxies. The average SFR of 'CAS-interacting' galaxies is only modestly enhanced compared to 'CAS non-interacting' galaxies, in agreement with the results from § 4.6.

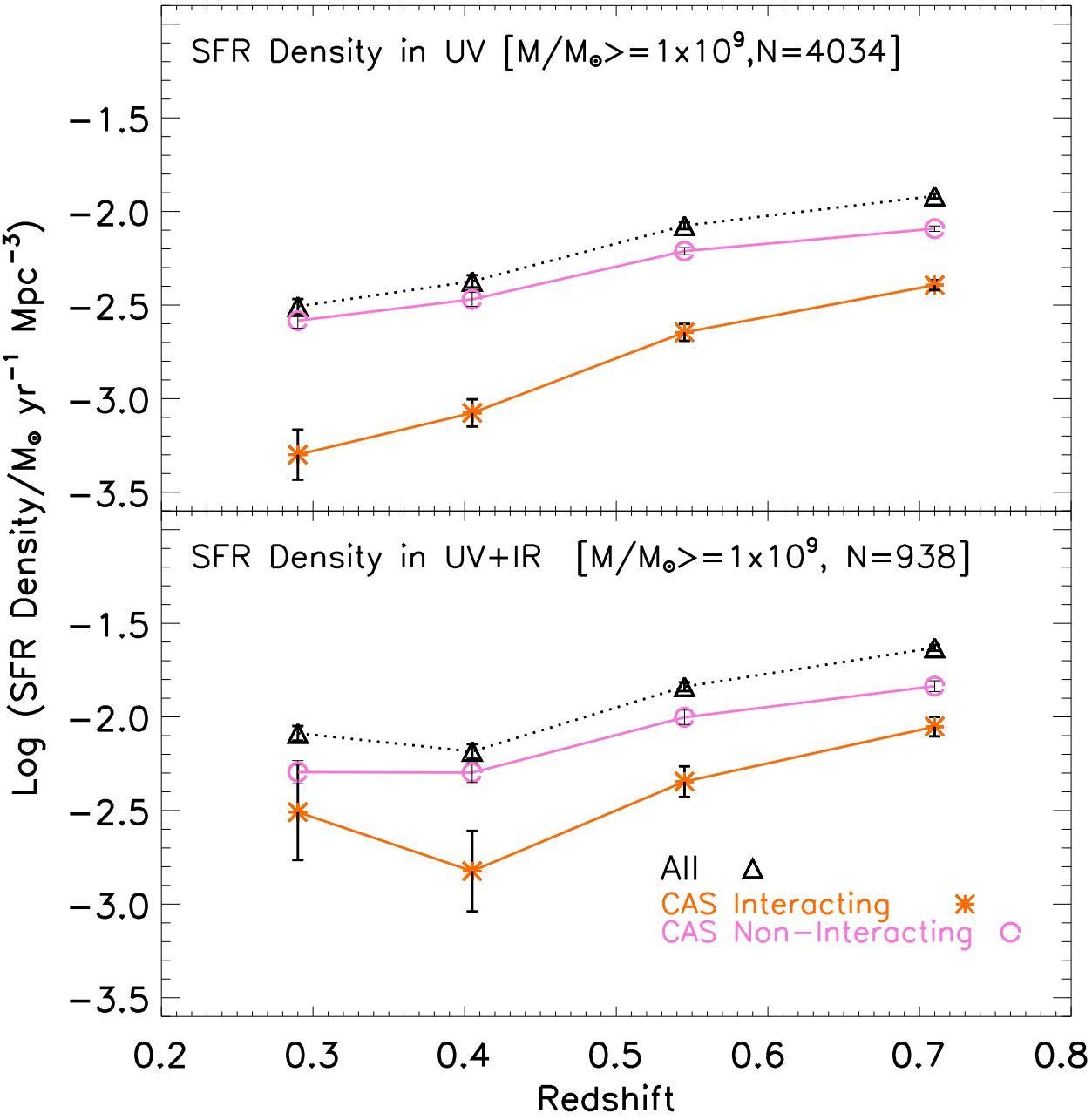

Fig. 17.— Same as in Fig. 15, but using the CAS merger criterion ($A > 0.35$ and $A > S$) to identify interacting galaxies. 'CAS-interacting' galaxies contribute only 16% to 33% of the UV SFR density and 22% to 38% of the UV+IR SFR density. While the upper limits of these values are slightly higher than those based on the visual types (Fig. 15), the 'CAS non-interacting' galaxies' clearly dominate the SFR density.

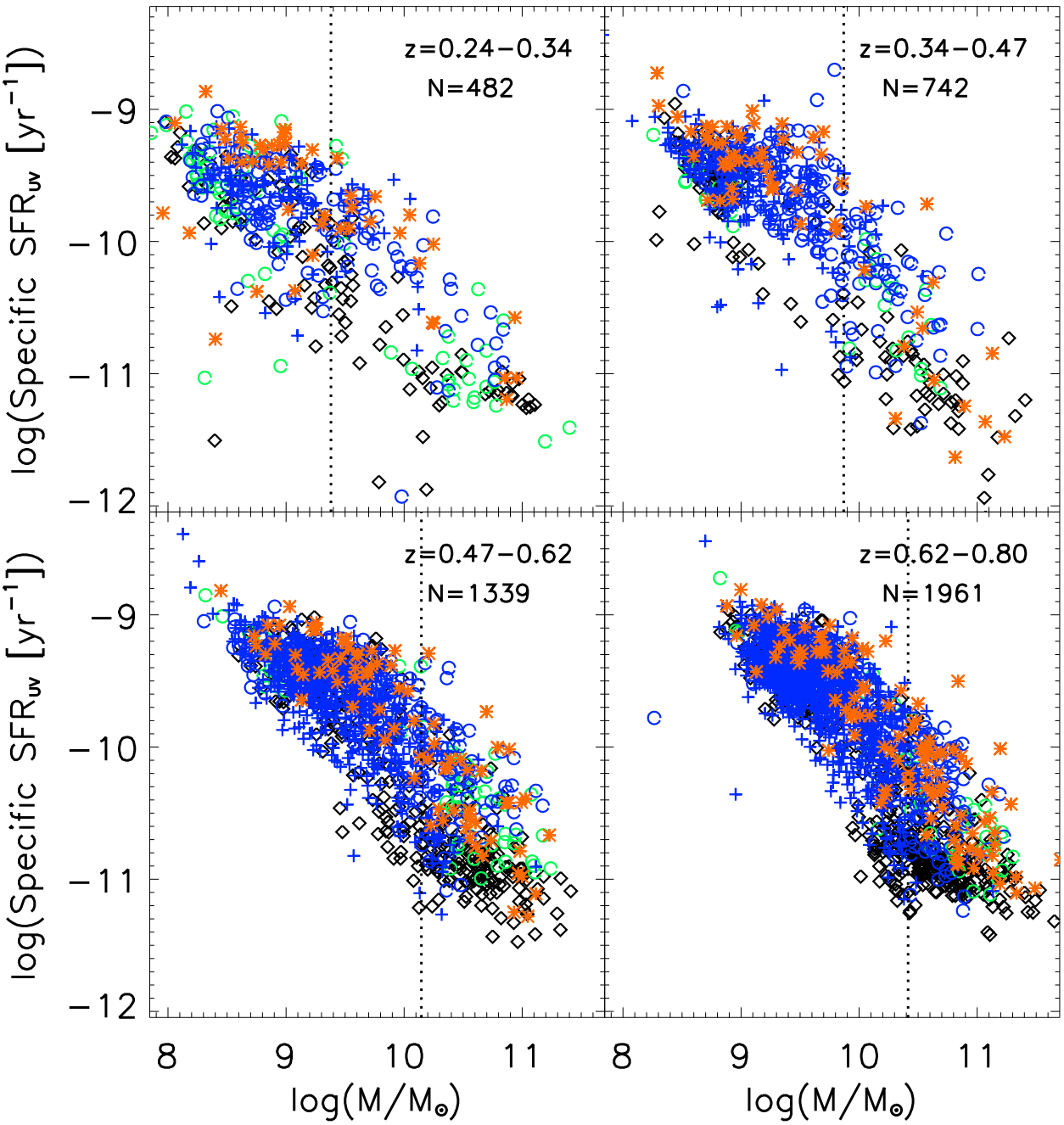

Fig. 18.— The specific SFR (defined as the SFR per unit stellar mass) based on UV data is plotted versus stellar mass. It ranges from 3×10^{-12} to 10^{-9} yr^{-1} and varies inversely with mass in all 4 redshift bins over $z \sim 0.24$–0.80. This is consistent with the idea that lower mass systems experience a larger fractional growth than high mass systems since $z < 1$, and that high mass systems have experienced the bulk of their stellar mass growth at earlier epochs ($z > 1$)

Table 1. Visual Interaction Fraction for High Mass ($M \geq 2.5 \times 10^{10}\ M_{\odot}$) Sample S1 [N=789]

(1)	Redshift bin	1	2	3	4
(2)	Redshift range	0.24–0.34	0.34–0.47	0.47-0.62	0.62–0.80
(3)	Lookback time [Gyr]	3.0–4.0	4.0–5.0	5.0–.6-0	6.0–7.0
(4)	$\lambda_{\rm rest}$ in F606W [Å]	4470–4414	4414–4023	4023–3651	3651–3286
(5)	Total no of galaxies	46	84	213	446
(6)	Fraction of Interacting	0.087±0.047	0.083±0.037	0.089±0.030	0.0807±0.025
(6a)	Lower limit on major merger fraction	0.022±0.021	0.035±0.022	0.014±0.009	0.011±0.006
(6b)	Lower limit on minor merger fraction	0.065±0.040	0.036±0.022	0.075±0.027	0.049±0.016
(6c)	Fraction of ambiguous minor/merger cases	0.00	0.012±0.012	0.00	0.020±0.008
(7)	Fraction of Non Interacting E-Sd	0.913± 0.241	0.869±0.229	0.878±0.229	0.785±0.205
(8)	Fraction of Non Interacting Irr1	0.000	0.024±0.018	0.009±0.007	0.025±0.010
(9)	Fraction of Compact	0.000	0.024±0.018	0.023±0.012	0.11±0.032

Note. — Rows are : (1) Redshift bin. (2) Range in redshift covered by the bin; (3) Range in lookback time covered by the bin; (4) Range in rest-frame wavelength traced by the F606W filter over the bin, assuming a pivot wavelength of 5915Å; (5) Total number of high mass galaxies per bin; (6) Fraction of galaxies visually classified as Interacting. These are likely candidates for interactions of mass ratio M1/M2> 1/10, including both major ($M1/M2 \geq 1/4$) and minor ($1/10 < M1/M2 \leq 1/4$) mergers; (6a) Lower limit on the fraction of galaxies undergoing major interactions/mergers; (6b) Lower limit on the fraction of galaxies undergoing minor interactions/mergers; (6c) Remaining fraction of galaxies that could be either major or minor interactions/mergers; (7-9) Fraction of Non-Interacting E-Sd, Non-Interacting Irr1, and Compact.

Table 2. Visual Interaction Fraction for $M \geq 1.0 \times 10^9\ M_\odot$ Sample S2 [N=3698]

(1)	Redshift bin	1	2	3	4
(2)	Redshift range	0.24–0.34	0.34–0.47	0.47-0.62	0.62–0.80
(3)	Lookback time [Gyr]	3.0–4.0	4.0–5.0	5.0–.6-0	6.0–7.0
(4)	$\lambda_{\rm rest}$ in F606W [Å]	4470–4414	4414–4023	4023–3651	3651–3286
		All [N=3698]			
(5)	Total no of galaxies	235	480	1117	1866
(6)	Fraction of Interacting	0.085±0.027	0.090±0.027	0.074±0.021	0.062±0.017
(6a)	Lower limit on major merger fraction	0.013±0.008	0.006±0.004	0.004±0.002	0.009±0.003
(6b)	Lower limit on minor merger fraction	0.038±0.016	0.021±0.008	0.021±0.007	0.017±0.005
(6c)	Fraction of ambiguous minor/merger cases	0.034±0.010	0.062±0.020	0.048±0.014	0.036±0.010
(7)	Fraction of Non Interacting E-Sd	0.850±0.220	0.846±0.220	0.796±0.207	0.793±0.206
(8)	Fraction of Non Interacting Irr1	0.064±0.023	0.052±0.017	0.108±0.030	0.064±0.018
(9)	Fraction of Compact	0.000	0.012±0.006	0.021±0.007	0.080±0.022
		Blue Cloud [N=2844]			
(10)	Total no of galaxies	154	332	876	1482
(11)	Fraction of Interacting	0.149±0.048	0.114±0.034	0.088±0.025	0.069±0.019
(11a)	Lower limit on major merger fraction	0.013±0.009	0.00	0.005±0.003	0.008±0.003
(11b)	Lower limit on minor merger fraction	0.046±0.020	0.024±0.010	0.023±0.008	0.016±0.005
(11c)	Fraction of ambiguous minor/merger cases	0.091±0.033	0.090±0.028	0.060±0.018	0.046±0.013
(12)	Fraction of Non Interacting E-Sd	0.753± 0.199	0.801±0.209	0.753±0.196	0.784±0.204
(13)	Fraction of Non Interacting Irr1	0.097±0.035	0.075±0.024	0.136±0.037	0.080±0.022
(14)	Fraction of Compact	0.000	0.009±0.006	0.023±0.008	0.067±0.018

Note. — Rows are : (1) to (9): As in Table 1, but for intermediate mass ($M \geq 1.0 \times 10^9\ M_\odot$) galaxies. However, note that the intermediate mass sample is incomplete for the red sequence. (10) to (14); Ditto, but for the blue cloud, where the sample is complete.

Table 3. Interaction fraction in GEMS F606W (V) and GOODS F850LP (z) [N=855]

		GEMS V Average	GOODS z Average	GOODS z SJ	GOODS z SM	GOODS z KP
(1)	Fraction f of interacting galaxies	0.046±0.007	0.049±0.007	0.051±0.007	0.057±0.008	0.038±0.006
(2)	Ratio of f in GOODS z to GEMS V	-	1.06±0.22	1.10 ±0.23	1.20±0.25	0.83 ±0.18

Note. — As a test for bandpass shift and surface brightness dimming, the table shows a comparison of the fraction of interacting galaxies based on visual classification of GEMS F606W images and deeper redder GOODS F850LP galaxies. The sample consists of the 855 intermediate mass ($M \geq 1.0 \times 10^9\ M_{\odot}$) galaxies at $z \sim$0.24 to 080, which are common to both GEMS F606W and GOODS F850LP surveys. Columns are: (2) Fraction f of interacting galaxies in GEMS F606W. The error bar only includes the binomial term $[f(1\text{-}f)/N)]^{1/2}$; (3) Average Fraction f of Interacting galaxies in GOODS F850LP based on results by classifiers (SJ,SM,KP), shown in columns 4–6.